

Improved *Hubble Space Telescope* Proper Motions for Tycho-G and Other Stars in the Remnant of Tycho’s Supernova 1572

L. R. Bedin¹, P. Ruiz-Lapuente^{2,3,4}, J. I. González Hernández^{5,6}, R. Canal^{7,3},
A. V. Filippenko⁸, J. Mendez^{9,7}

¹*INAF-Osservatorio Astronomico di Padova, Vicolo dell’Osservatorio 5, I-35122 Padova, Italy*

²*Instituto de Física Fundamental, Consejo Superior de Investigaciones Científicas, c/Serrano 121, E-28006 Madrid, Spain*

³*Institut de Ciències del Cosmos (UB-IEEC), c/ Martí i Franqués 1, E-08028 Barcelona, Spain, E-mail: pilar@am.ub.es*

⁴*Max-Planck Institut für Astrophysik Karl Schwarzschildstrasse 1 D 85748 Garching Germany*

⁵*Instituto de Astrofísica de Canarias, E-38205 La Laguna, Tenerife, Spain*

⁶*Departamento de Astrofísica, Universidad de La Laguna, E-38206 La Laguna, Tenerife, Spain*

⁷*Departament d’Astronomia i Meteorologia, Universitat de Barcelona, c/ Martí i Franqués 1, 08028 Barcelona, Spain*

⁸*Department of Astronomy, University of California, Berkeley, CA 94720–3411, USA*

⁹*Isaac Newton Group of Telescopes, PO Box 321, E-38700 Santa Cruz de la Palma, Spain*

Accepted 2013 December 18. Received 2013 December 18; in original form 2013 May 6

ABSTRACT

With archival and new *Hubble Space Telescope* observations we have refined the space-velocity measurements of the stars in the central region of the remnant of Tycho’s supernova (SN) 1572, one of the historical Galactic Type Ia supernova remnants (SNRs). We derived a proper motion for Tycho-G of $(\mu_{\alpha \cos \delta}; \mu_{\delta})_{J2000.0} = (-2.63; -3.98) \pm (0.06; 0.04)$ [formal errors] $\pm (0.18; 0.10)$ [expected errors] mas yr⁻¹. We also reconstruct the binary orbit that Tycho-G should have followed if it were the surviving companion of SN 1572. We redetermine the Ni abundance of this star and compare it with new abundance data from stars of the Galactic disk, finding that [Ni/Fe] is about 1.7 σ above the Galactic trend. From the high velocity ($v_b = -50 \pm 14$ km s⁻¹) of Tycho-G perpendicular to the Galactic plane, its metallicity, and its Ni excess, we find the probability of its being a chance interloper to be $P \lesssim 0.00037$ at most. The projected rotational velocity of the star should be below current observational limits. The projected position of Tycho-G is, within the uncertainties, consistent with the centroid of the X-ray emission of Tycho’s SNR; moreover, its brightness is generally consistent with the post-explosion evolution of the luminosity of a SN companion. Among the other 23 stars having $V < 22$ mag and located within 42'' from the X-ray centroid, only 4 are at distances compatible with that of the SNR, and none of them shows any peculiarity. Therefore, if even Tycho-G is *not* the surviving companion of SN 1572, the absence of other viable candidates does favor the merging of two white dwarfs as the producer of the SN.

Key words: Astrometry – binaries: close – supernova remnants: individual (SNR 1572)

1 INTRODUCTION

Type Ia supernovae (SNe Ia) have long been recognised as being close binary systems where one of the stars, a carbon-oxygen white dwarf (C+O WD), undergoes a thermonuclear runaway after reaching explosive conditions at its centre (e.g., Branch et al. 1995, and references therein). The physics of the explosion is determined by both components of the system. While the ejecta left by the explosion have

been studied in great detail, the direct search for the companion is a relatively new approach (Ruiz-Lapuente 1997) that has already started to give results (Ruiz-Lapuente et al. 2004, hereafter RL04; González Hernández et al. 2009, hereafter GH09; Schaefer & Pagnotta 2012; Edwards et al. 2012; González Hernández et al. 2012; Kerzendorf et al. 2012).

SNe Ia are the best cosmological distance indicators, and they were used to discover the accelerating expan-

sion of the Universe (Riess et al. 1998; Perlmutter et al. 1999). While they are well characterised for empirical use as cosmological probes, there are still significant gaps in our theoretical understanding of them. In principle, SNe Ia can be produced through two different channels: the single-degenerate (SD) channel and the double-degenerate (DD) channel (Whelan & Iben 1973; Webbink 1984; Iben & Tutukov 1984; Livio & Truran 1992; Branch et al. 1995; Ruiz-Lapuente 1997; Livio 2000; Ruiz-Lapuente et al. 2003). In the SD channel, the progenitor WD approaches the Chandrasekhar mass by accreting matter, in a close binary system, from a companion star that is thermonuclearly evolving (the nondegenerate component). The companion could be a giant, a subgiant, or a main-sequence star. In the DD channel, the binary consists of two WDs which eventually merge, thereby giving rise to the explosion; no bound object is left. In the SD channel, on the other hand, the companion star should survive the explosion and show distinguishing properties. The predictions of how the companion star would look after the impact depend on the star's physical properties before the explosion (Canal et al. 2001; Livio 2000; Marietta et al. 2000; Podsiadlowski 2003; Pakmor et al. 2011; Pan, Ricker, & Taam 2012a,b; Shappee et al. 2013; Liu et al. 2012, 2013).

To test the binary scenario, we observed and modeled stars within the 15% inner radius of Tycho's SN 1572 (RL04). Previous research (Ruiz-Lapuente 1997; Canal et al. 2001; Ruiz-Lapuente et al. 2003) had pointed out that the most salient feature of the surviving companion star should be peculiar velocities with respect to the average motion of the other stars at the same location in the Galaxy (mainly due to disruption of the binary), detectable through radial-velocity and proper-motion measurements, and perhaps also signs of the impact of the SN ejecta. The latter can be twofold. First, mass should have been stripped from the companion and thermal energy injected into it, possibly leading to the expansion of the stellar envelope and making the star have a lower surface gravity (Marietta et al. 2000; Podsiadlowski 2003). Second, depending on the interaction with the ejected material, the surface of the star could be contaminated by the slowest-moving ejecta (made of Fe and Ni isotopes). Determination of the metallicity is also needed in order to exclude the star belonging to the halo or thick disk. The observations in RL04, therefore, were designed along these lines.

The search for the binary companion of Tycho's SN 1572 has produced a likely candidate: a G-type subgiant star labelled Tycho-G (RL04, GH09). The star is relatively close to the centre of the supernova remnant (SNR), its distance is compatible with being inside the SNR, it has significantly higher radial velocity and proper motion (PM) than stars at the same location in the Galaxy, and it shows signs of pollution from the SN ejecta. The radial velocity, $v_r = -80 \pm 0.5 \text{ km s}^{-1}$ in the Local Standard of Rest, is about 2σ above the average for stars at the distance of the SNR. Especially significant, however, is the PM measured with the *Hubble Space Telescope* (*HST*) in programs GO-9729 (Cycle 12) and GO-10098 (Cycle 13): $\mu_l = -2.6 \pm 1.3 \text{ mas yr}^{-1}$, $\mu_b = -6.1 \pm 1.3 \text{ mas yr}^{-1}$. At a distance of 3 kpc, this gives a tangential velocity of $94 \pm 27 \text{ km s}^{-1}$, but the disk velocity dispersion is much smaller. It seems very difficult, therefore, to account

for the observed PM, except through some sort of binary interaction.

This point was later challenged by Kerzendorf et al. (2009, hereafter K09). From comparison of a photographic plate taken in 1970 with the Palomar 5-m telescope and a CCD image taken in 2004 (used in RL04) with the 2.5-m Isaac Newton Telescope, K09 concluded that no significant PM was detected: $\mu_l = -1.6 \pm 2.1 \text{ mas yr}^{-1}$, $\mu_b = -2.7 \pm 1.6 \text{ mas yr}^{-1}$. However, the measurements prior to the present work (RL04), also based on *HST* images, again gave a significant PM: $\mu_{\alpha \cos \delta} = -2.3 \pm 2.8 \text{ mas yr}^{-1}$, and $\mu_\delta = -4.8 \pm 2.8 \text{ mas yr}^{-1}$ (maximal external errors using the three epochs 2003, 2004, and 2005). More recently, a PM of about 5 mas yr^{-1} was also obtained using the same publicly available Cycle 16 *HST* data (Kerzendorf et al. 2013, hereafter K13), but the error bars remain quite large.

Any improvement in the PM measurements of the stars significantly increases information on the pre-explosion binary system. The peculiar velocity of a surviving companion would correspond largely to its orbital velocity just before the explosion, since the kick due to the impact from the ejecta is a secondary effect (Marietta et al. 2000). From the mass of the companion (the WD being near the Chandrasekhar mass when it explodes), the orbit prior to the explosion can be reconstructed, if we assume that both the radial and tangential velocities of the centre of mass of the binary were typical for the distance and Galactic latitude of the SNR.

With the present work we aim to refine the evolutionary path to the explosion of SN 1572 by reducing by an order of magnitude the uncertainties in the PMs of the stars. This improvement is now possible because almost eight years have passed between the ACS/WFC 2003 images and the new ones (taken in late 2011, during *HST* Cycle 19).

After the publication of RL04, there were claims that the proposed companion of SN 1572, Tycho-G, was a giant star, with $\log(g/\text{cm-s}^{-2}) = 1.9 \pm 0.4$ dex and at a distance ~ 10 kpc (Schmidt et al. 2007). Keck HIRES spectra taken in 2006 did show that Tycho-G is, in fact, rather similar to the Sun, as was already discussed by RL04. The analysis of these new observations (GH09) confirmed that it is a G-type subgiant, with $T_{\text{eff}} = 5900 \pm 100 \text{ K}$, $\log(g/\text{cm-s}^{-2}) = 3.85 \pm 0.30$ dex, and $[\text{Fe}/\text{H}] = -0.05 \pm 0.09$. It is thus neither a halo star nor a typical thick-disk star. Its distance is entirely compatible with that of the SNR (around 3 kpc). Moreover, a chemical abundance analysis showed a clear excess of Ni (and, to a less significant extent, of Co), which could point to possible contamination of the star's surface layers by the SN ejecta (GH09).

Additional support for the single-degenerate origin of Tycho's SN has been obtained recently from X-ray observations (Lu et al. 2011), and the characteristics of the binary have been partially reconstructed based on the results of RL04.

Concerning the PM issue, very recently K13 have also analysed our now publicly available GO-9729 and GO-10098 *HST* images and derived values in agreement with previous results by RL04. In particular, they confirm the high velocity of Tycho-G, perpendicular to the Galactic plane. In the present work, in which we use *HST* observations spanning nearly 8 years, a similar result is obtained, but with an almost tenfold precision.

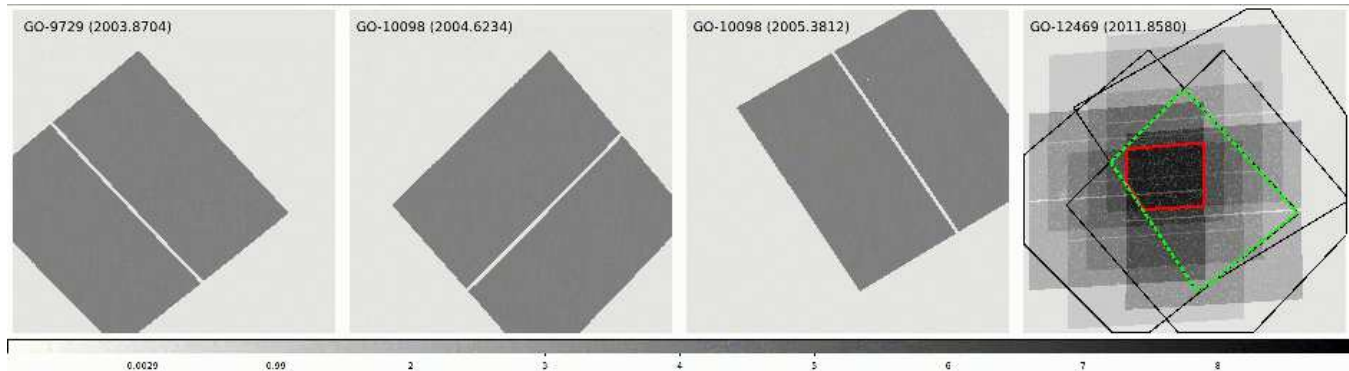


Figure 1. Depth-of-coverage map for the ACS/WFC and WFC3/UVIS epochs used in this work. Clearly, the WFC3/UVIS GO-12469 epoch (far-right panel) is the most dithered one, and it provides the best overlap with the other epochs. Solid lines show the regions of interest of previous epochs, while a green dashed line delimits the region for which four epochs are available. A subregion, marked in red, indicates where we have the maximum number of deep exposures in all 4 epochs; sources within it have the best PM measurements.

Table 1. F555W data used in this work.

Epoch (date) / camera	$N_{\text{exp}} \times \text{exp-time}$ (s)	Dataset
2003.8704	4×360	GO-9729
13 Nov. 2003	3×10	GO-9729
ACS/WFC	3×0.5079	GO-9729
2004.6234	4×360	GO-10098
15 Aug. 2004	3×10	GO-10098
ACS/WFC	3×0.5079	GO-10098
2005.3812	4×360	GO-10098
19 May 2005	3×10	GO-10098
ACS/WFC	3×0.5079	GO-10098
2011.8580	1×373	GO-12469
9 Nov. 2011	5×372	GO-12469
WFC3/UVIS	2×21	GO-12469

Other stars close to the centre of Tycho’s SNR are occasionally suggested as possible companions, such as Tycho-E (Ihara et al. 2007), which is, in fact, a double-lined binary (see GH09), or Tycho-B (K13) because of its high rotational velocity, which is, in fact, completely normal for its type: an A8–A9 main-sequence star (Abt & Morrell 1993, 1995). More complete knowledge of the PMs of all stars in the field, in addition to Tycho-G, was thus crucial (see Sec. 9).

Here we first present and discuss the new astrometric work (Sec. 2 and 3). In Section 4 we redetermine the Ni abundance of Tycho-G, using the same HIRES spectrum as in GH09 but a new procedure, and we compare it with the Galactic trend, also defined by new high-quality data. We reconstruct the binary orbit of the star (Sec. 5), assuming Tycho-G to be the surviving SN companion, and from that we deduce its radius at the time of the explosion, when it was filling its Roche lobe. In Section 6, we discuss the kinematics of Tycho-G and its significance. We evaluate the probability of picking at random a star that combines all of its characteristics (Sec. 6). Sections 7 and 8 briefly discuss the uncertainties in the exact site of the SN explosion and the luminosity evolution of a SN companion after the impact

of the SN ejecta. In Section 9, the data on the other 23 stars with $V < 22$ mag and within $42''$ of the centroid of the SNR X-ray emission are presented and discussed. We summarize our conclusions in Section 10.

2 OBSERVATIONS AND DATA REDUCTION

The observations used to derive the PM measurements presented here come from *HST* programs GO-9729, GO-10098, and GO-12469 (PI Ruiz-Lapuente), which span ~ 8 yr. Data were collected with both the Wide Field Channel (WFC) of the Advanced Camera for Surveys (ACS), and the Ultraviolet-Visual (UVIS) channel of the Wide Field Camera 3 (WFC3). All of these images were taken with the filter F555W, available for both cameras. However, we note that the two total transmissions (instrument+filter) are slightly different. For precise astrometric measurements and a more accurate assessment of the uncertainties, we took particular care to dither our new WFC3/UVIS images properly, with both large whole-pixel and fractional-pixel offsets (following the general recipes given by Anderson & King 2000). This was not the case during previous ACS/WFC epochs, resulting in some limitations to our achieved accuracies. Table 1 lists both the ACS/WFC and WFC3/UVIS observations, while Fig. 1 shows the depth-of-coverage map for each of the four epochs, after being transformed into the same reference system.

2.1 Correction for Imperfect CTE

CCD detectors in the harsh radiation environment of space suffer degradation owing to the impact of energetic particles, which displace silicon atoms and create defects. These defects temporarily trap electrons, resulting in charge transfer efficiency (CTE) losses and in trailing of the sources (because electrons are released at a later time). These effects have a major impact on astrometric projects (Anderson & Bedin 2010).

In this work, every single ACS/WFC image employed was treated with the pixel-based correction for imperfect CTE developed by Anderson & Bedin (2010). The algorithm

WFC3/UVIS REFERENCE FRAME [2011.858]

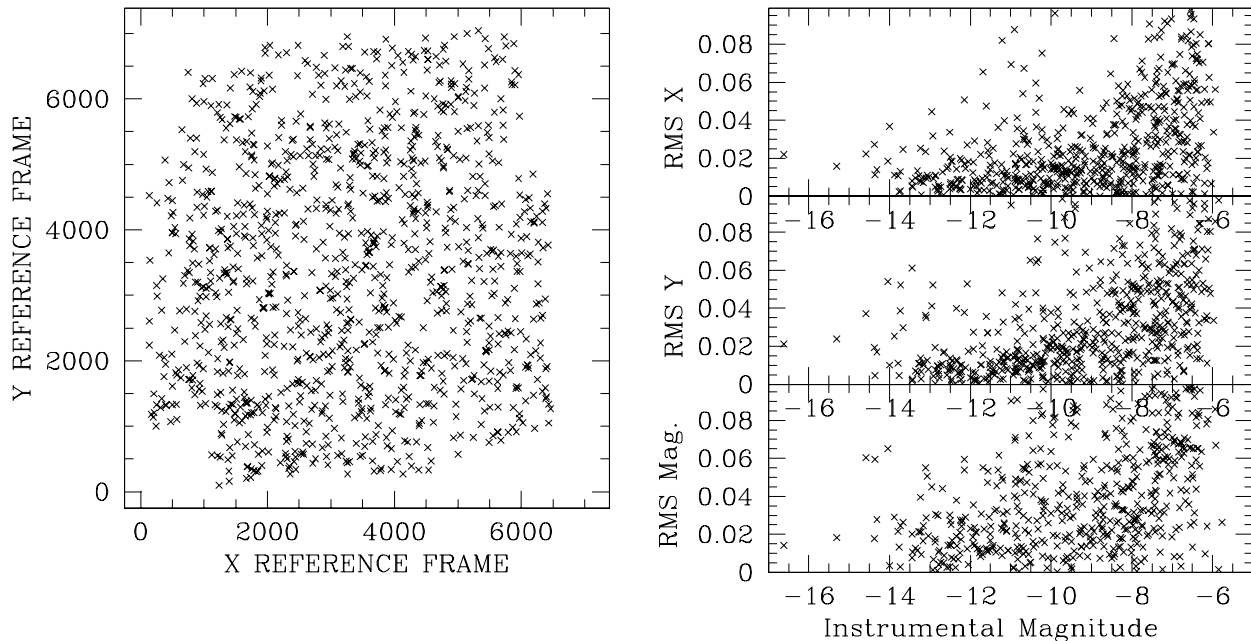


Figure 2. *Left:* Spatial distribution of the reference frame built from WFC3/UVIS data. *Right:* The RMS in X -coordinate position (*top*), Y -coordinate position (*middle*), and magnitude (*bottom*) as measured in single images (from 2, up to 8). These RMS estimates have different noise, depending on the available number of data points and the brightness of the sources. All positions are in units of WFC3/UVIS pixels.

is now improved¹ and directly included in the ACS pipeline. Standard calibrated products are produced both with (`_flc` exposures) and without (`_flt` images) this correction. This correction proved to be effective in restoring fluxes, positions, and the shape of sources, and reducing systematic effects of imperfect CTE even in the worst case of extremely low backgrounds (Anderson & Bedin 2010; Ubeda & Anderson 2012). The WFC3 team is still working to develop and calibrate a similar capability for UVIS; therefore, no CTE mitigation was operated on WFC3/UVIS images in this work. However, the relative “youth” of UVIS’s CCDs and the large-dither strategy of our new observations provide a good handle on the astrometric biases resulting from imperfect CTE, as well as on other systematic sources of errors.

2.2 Fluxes and Positions in the Individual Images

We measured positions and fluxes for every star in every `_flc` ACS/WFC exposure, using a library of spatially variable effective point-spread functions (PSFs) and the software programs documented by Anderson & King (2006). Unfortunately, due to the sparseness of the Tycho-G field, it was

not possible to perturb the PSFs to account for small focus variations. (We will see in Sec. 3.4 how we have mitigated this and other systematic biases in our astrometry.) As in Bedin et al. (2003, 2006), we used the best available average distortion corrections (Anderson 2002, 2005) to correct the raw positions and fluxes of sources that we had measured within each individual ACS/WFC `_flc` exposure.

Positions and fluxes of sources in each WFC3/UVIS `_flt` image were obtained with software that is adapted from the program `img2xym_WFI` (Anderson et al. 2006). Astrometry and photometry were then corrected for pixel area and geometric distortion using the best available average distortion corrections and library PSFs (Bellini & Bedin 2009; Bellini et al. 2011).

3 ASTROMETRY AND PROPER MOTIONS

To derive proper motions, we essentially follow the detailed procedures given by Anderson & van der Marel (2010, hereafter Av10) to measure the internal motions of the stars in the core of the populous globular cluster ω Centauri. However, we need to take into account that the Tycho-G field has major differences with respect to the field studied by Av10.

Our astrometric measurements, like those of Av10, are relative to a group of objects in the observed field. As a reference, Av10 used cluster members; there are hundreds of stars per square arcminute having high signal-to-noise ratios (S/N), all at a common distance, and sharing a common PM

¹ The pixel-based CTE correction scheme based on the work of Anderson & Bedin (2010) has been modified to include the time- and temperature-dependences of CTE losses (Ubeda & Anderson 2012). An improved correction at low signal and background levels has also been incorporated, as well as a correction for column-to-column variations.

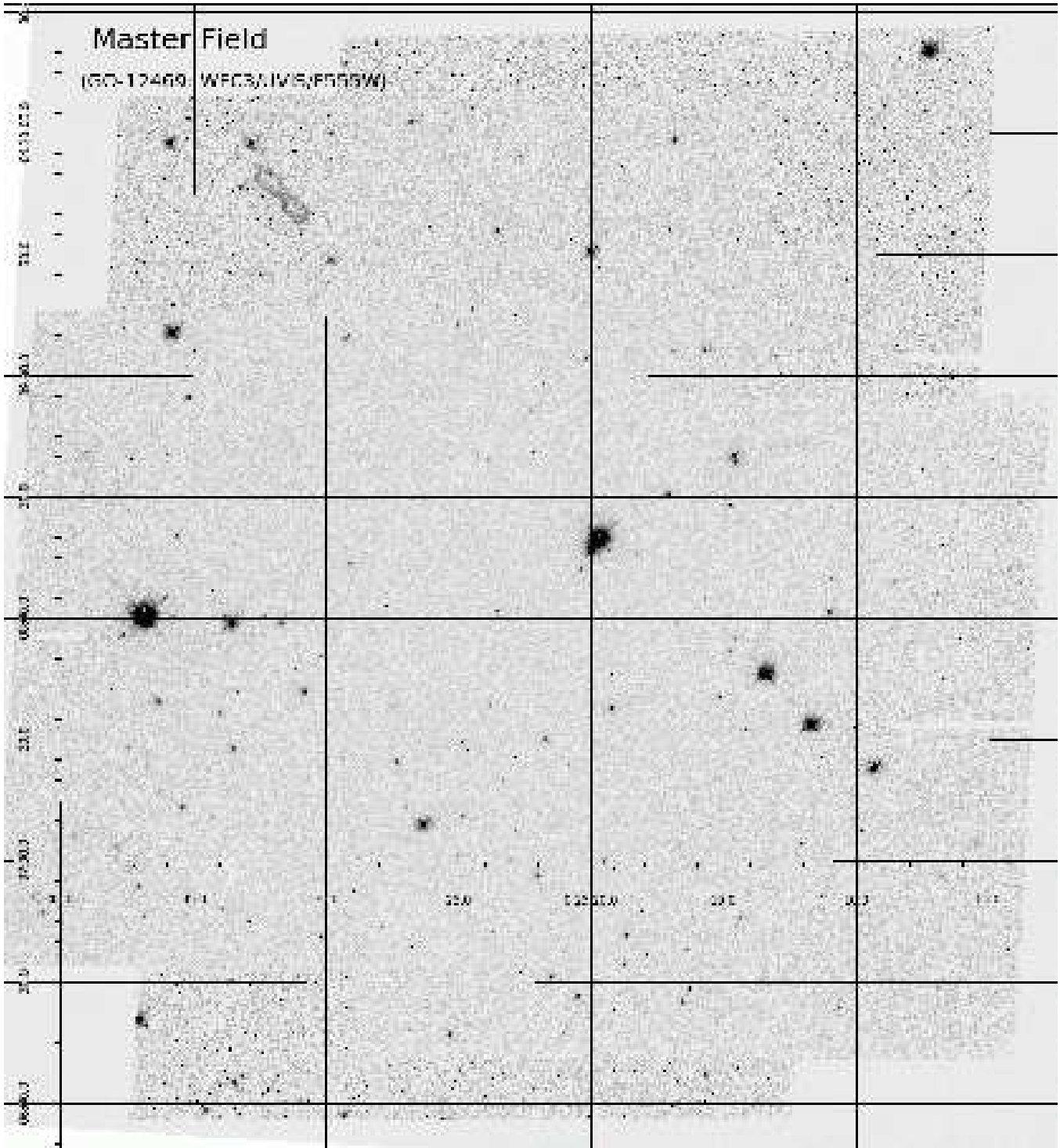


Figure 3. Stack of the deep WFC3/UVIS/F555W $_fit$ images from GO-12469 transformed into the reference frame.

to within a few 0.1 mas yr^{-1} (the internal velocity dispersion of $\omega \text{ Cen}$ is less than 20 km s^{-1}).

By contrast, our Tycho-G field is sparsely populated, with only a few objects per square arcminute. Furthermore, the reference stars are at different distances and have different PMs. We also note that no obvious and suitable background object is present in our field, as a result of the high extinction at low Galactic latitudes ($b \approx 1.5^\circ$). In our Tycho-

G field, the uncertainties in our PMs are dominated by the PM dispersions of the stars with respect to which we measure the positions at the different epochs, even selecting stars that moved the least with respect to each other. Nonetheless, our long temporal baseline of $\sim 8 \text{ yr}$ improves the final precision to levels comparable to those reached by Av10.

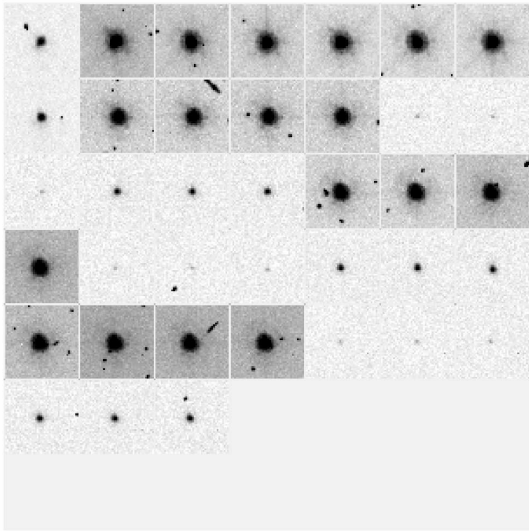


Figure 4. From left to right, and from top to bottom, a mosaic of the 40×40 pixels around Tycho-G in each of the 38 images available to us (see Table 1). The first eight are from the UVIS epoch, and the next 30 from ACS (specifically, 10 collected in 2003, then 10 from 2004, and the last 10 from 2005).

3.1 The Reference Frame

The first important step is to build a distortion-free *reference frame* using all of the images taken within a chosen epoch (the *reference epoch*), with respect to which we will later perform *all* of the relative measurements. For this task we selected our recent WFC3/UVIS epoch, as this epoch is the one with the largest number of deep observations, optimal dithering, and covering the largest fraction of the other previous epochs (see Fig. 1). In addition, because of its better pixel sampling, WFC3/UVIS intrinsically provides better imaging astrometry (~ 0.3 mas; Bellini et al. 2011) compared with ACS/WFC (~ 0.5 mas; Anderson & King 2006).

To build the reference frame, we began by identifying bright, isolated, and unsaturated sources measured within each WFC3/UVIS `.flt` image of program GO-12469. Among these, we then selected those having a stellar profile. To measure the stellarity of objects, we use the “quality-fit” (q-fit) parameter described by Anderson et al. (2008), which essentially quantifies how close the distribution of the observed pixel values resembles the local PSF model. This selection allowed us to immediately reject most cosmic ray (CR) hits, warm pixels, artifacts, and potentially also extended nonstellar objects. With caution, this enabled us to use those portions of the field observed only once in the reference epoch (i.e., those regions for which there is only one exposure in the reference epoch).

We initially took as a reference the distortion-corrected positions measured in the deep image `iboy01mhq`, which is at the centre of the WFC3/UVIS dither pattern, and linearly transformed the star positions (distortion-corrected) from all of the other images into that frame. We then determined an average position for each star that was found in at least

five exposures. In doing this, we used the most general linear transformations (6 parameters).

To improve this reference frame, we found a linear transformation from each exposure into the new frame, based on the positions of common stars. For each star in the reference frame, we thus had between five and eight estimates for its position (depending on how many images overlapped at that point), and we averaged these positions together to improve the reference frame. After a few such iterations, the root-mean square (RMS) of these multiple (and dithered) observations was less than 0.01 pixels for the brightest stars (with 5 or more observations).

To extend the reference frame where there are fewer than five images, we used the same transformations obtained above to include the objects with faint magnitudes and a stellar profile, and stars measured only in four, three, two, and one image. The resulting reference frame contains 1148 objects (a few of which are artifacts or remaining CRs). Its spatial distribution, together with the RMS in magnitude and in X and Y positions, are shown in Fig. 2.

3.2 Absolute Astrometry

As extensively discussed in Sec. 3.4, the adopted geometric distortion correction is just an average solution, and from frame to frame there are sizable changes. This is particularly true for the linear terms, which contain the largest portion of the variations. So far, in deriving the reference frame, we used 6-parameter linear transformations to register the distortion-corrected positions measured in each frame to the distortion-corrected positions measured in the reference image `iboy01mhq`; the linear-term variations with respect to the reference image were completely absorbed by the 6 parameters. Therefore, the astrometric zero points, plate scales, orientations, and skew terms of our adopted reference frames are still not calibrated to an absolute reference system.

We used sources in common between our reference frame and the Two Micron All Sky Survey (2MASS, Skrutskie et al. 2006) to determine the unconstrained linear terms. Within our Tycho-G region we found ~ 80 2MASS point sources in common with our reference frame which we used to calibrate our linear terms. The constrained linear terms enabled absolute astrometry accurate to $\sim 0.2''$. As previously mentioned, the relative positions of stars are much more accurate than their absolute zero points. The nonlinear part of the ACS/WFC and WFC3/UVIS distortion solutions is accurate to ~ 0.01 original-size WFC3/UVIS pixel (~ 0.4 – 0.5 mas) in a global sense (Anderson & King 2006; Bellini et al. 2011), roughly the random positioning accuracy with which we can measure a bright star in a single exposure. Recently, it has been discovered that the linear terms of the ACS/WFC distortion solution have been changing slowly over time (Anderson 2007). Even if this were the case also for WFC3/UVIS, we note that in our procedure the linear terms are constrained by the 2MASS catalog. The absolute coordinates are referred to equinox J2000.0, with positions given at the reference epoch, 2011.858.

3.3 Image Stack

With the transformations from the coordinates of each image into the reference frame it becomes possible to create a

stacked image of the field within each epoch. The stack provides a representation of the astronomical scene that enables us to independently check the region around each source at each epoch. The stacked images are $15,000 \times 15,000$ super-sampled pixels (by a factor 2; i.e., $20 \text{ mas pixel}^{-1}$), and corresponding to $\sim 5' \times 5'$. The stack for the WFC3/UVIS 2011 epoch is shown in Fig. 3. We have included in the header of the image, as World Coordinate System (WCS) keywords, our absolute astrometric solution based on the 2MASS point-source catalog, as described in the previous section. As part of the material provided in this paper, we give the astrometrised stack-image for the reference epoch electronically online.

In Fig. 4, we show a mosaic of the 40×40 pixel field for all 38 images, centred on Tycho-G.

3.4 Boresight Correction

Positional imaging astrometry in *HST* images is so precise that it allows us to appreciate small variations from frame to frame, even if collected consecutively within a same orbit. For example, the velocity of *HST* around the Earth ($\pm 7 \text{ km s}^{-1}$) causes light aberration, inducing plate-scale variations up to 5 parts per 100,000 (Cox & Gilliland 2003) that can be measured clearly (Anderson et al. 2007; Bellini et al. 2011).

There are also less predictable time-dependent changes caused by the temporal variation of the *HST* focus. These focus variations are correlated with thermal variations induced by the angles between the Sun and the telescope tube (the so-called “breathing”); they result in changes in the geometric distortion and in position-dependent PSF variations, which in turn are the result of a complicated interplay between aberrations and charge diffusion across the detector (Jee et al. 2007). Therefore, the astrometric distortion solutions provided by Anderson & King (2006) for ACS/WFC and by Bellini et al. (2009, 2011) for WFC3/UVIS should be intended only as *average* geometric distortion solutions. The same considerations are also valid for the adopted library (and thus *average*) PSFs. Our estimated positions could thus change appreciably from frame to frame when using library PSFs and average distortion solutions.

To account for these small but sizable effects, Av10 introduced local adjustments to the measured positions, which they call “boresight” corrections. These corrections are determined for each star in each frame as follows. For each exposure that included the star, we calculate a robust average offset between the globally transformed (into the reference frame) positions of the neighbouring stars and the average reference-frame positions of the same neighbouring stars. This average offset provides the correction to the transformed position of the target star for that exposure. Hence, the reference frame contributes only to the plate scale and orientation (see Av10 for details). For images collected in the same epoch as the reference frame, we selected among neighbouring stars only those having positions within 0.05 WFC3/UVIS pixels from their positions in the master frame, but within 1 WFC3/UVIS pixel for the other ACS/WFC epochs. (We must be more generous from epoch to epoch, as the displacements also contain the intrinsic motions of stars.)

In the case of Av10 these corrections were extremely local, over a few tens of pixels, since the set of reference stars

was very dense. But owing to the sparseness of the Tycho-G field, our local set (used for the boresight corrections) includes neighbouring stars up to 1000 UVIS pixels from the target stars (i.e., a $\sim 1/4$ of a WFC3/UVIS field), thereby making these corrections not very “local.” Thus, our boresight correction will remove only residuals with this spatial scale. Also, the boresight correction is calculated only if at least 6 suitable objects are available within 1000 UVIS pixels from the target. Typically we had ~ 40 objects, but for short exposures the paucity of stars forced us to accept as few as 6.

The top panels in Fig. 5 show the “plain” (or raw) residuals between positions measured in individual frames and the reference frame. The corresponding boresight corrections are given in the second panels from the top, while the “boresight-corrected” residuals are shown in the third panels. The bottom panels display the spatial distributions of the sources with respect to the reference frame. We note that these boresight corrections are small within the reference epoch, of order ~ 0.01 WFC3/UVIS pixels ($\sim 0.4 \text{ mas}$), but they can be as large as 0.1 pixels ($\sim 4 \text{ mas}$) from one epoch to another.

Here we must make an important consideration concerning the achievable accuracy of our PMs (μ), which are described in the next section. The accuracies we can hope to achieve ($\overline{\sigma_{1D\mu}}$) are ultimately set by *both* the PM dispersion ($\sigma_{1D\mu}$) and the number of neighbouring stars (N_{used}) used to derive the boresight corrections. These accuracies can be formulated in the relation [for each of the two 1D PM components, $(\mu_{\alpha \cos \delta}, \mu_{\delta})$] as

$$\overline{\sigma_{1D\mu}} = \frac{\sigma_{1D\mu}}{\sqrt{N_{\text{used}} - 1}}. \quad (1)$$

This statistical “kinematic noise” of the network of stars, whose positions are not fixed with respect to each other, dominates our uncertainties. We will further discuss this issue in Sec. 3.5.1, where we also explicitly quantify the values of $\overline{\sigma_{1D\mu}}$ for Tycho-G.

3.5 Proper-Motion Measures

In Fig. 6 we summarise our multi-epoch fit to the motion of Tycho-G. The bottom and top halves refer to the $\alpha \cos \delta$ and δ motions, respectively. In each half, the top panel shows the boresight-corrected displacements as measured at the various epochs (i.e., residuals as those in the third-panel from top in Fig. 5). The displacements are with respect to the reference frame (in mas units), and the time (in years) is relative to our reference epoch (2011.8580). The data points from deep exposures are indicated with (red) open circles, while those from short exposures with (red) open squares. Data points from saturated images are not used. The blue lines are our weighted best *linear* fit to the data points, where for weights we adopted the raw fluxes measured in the individual images. In this way, when both short and long exposures are available (as is the case for Tycho-G), data points coming from short exposures receive negligible weights. Indeed, short exposures are the most affected by CTE, and by statistical limitations related to the paucity

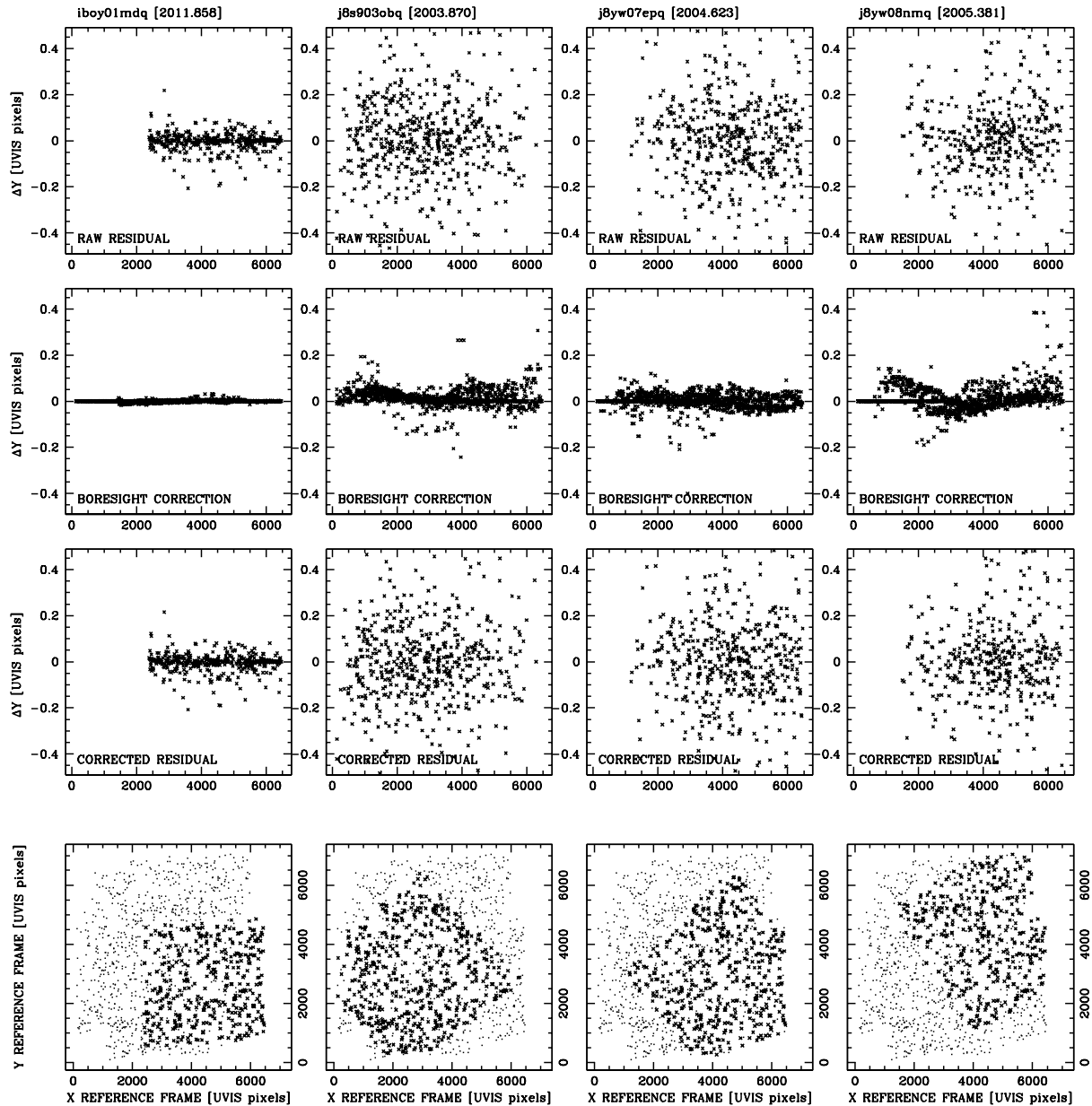


Figure 5. Each column of panels refers to the first deep image of each epoch. *Top panels:* As a function of the X -coordinate in the reference frame, we show the Y -residual (raw) between positions of stars measured in an individual image (distortion corrected and linearly transformed into the reference frame), and its Y -position in the reference frame. *Second panels:* The local “boresight” correction used for each star (see text) to remove residuals in the distortion correction. *Third panels:* The residuals after making these local adjustments. Those in the left column (relative to image *iboy01mdq*) show only distortion errors (plus random errors) but have no PMs, as the reference frame is based on images taken at that epoch. For exposures taken at the other epochs (other columns), these residuals contain both distortion errors and actual PMs, and therefore show larger scatter than in the left column. Note that many of these point sources are faint stars that have large random errors due to the low S/N. Also, these are single-image measurements, which could be affected by CRs and other artifacts. *Bottom panels:* The location of the image stars (crosses) with respect to the master-frame stars (thin dots).

of reference stars having good S/N.² Therefore, the slopes

² The disagreement between the motions inferred from short and long exposures for the case of Tycho-G should be used as a warning for potential systematics in the motions of other objects based only on short exposures.

of the blue lines are our estimates for the PMs of Tycho-G. These are labeled in the figure as $\mu_{\alpha \cos \delta}$ and μ_{δ} with their formal errors. The average of the displacements should be null at the reference epoch.

Note that in fitting the data, we let the positions at the reference epoch float freely; consequently, δ_0 and α_0 in-

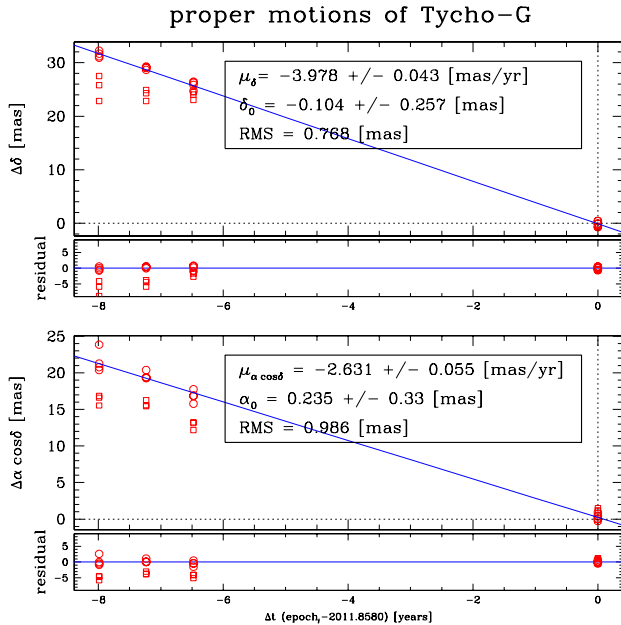


Figure 6. Multi-epoch fit of the PMs (and residuals) for Tycho-G (bottom half for the motion in $\alpha \cos \delta$, and top half for the motion in δ). In each half, the upper panel shows the displacement (in mas) for the four epochs as a function of time from the reference epoch (in years). The blue line is the weighted best fit to the data points (circles from deep exposures and squares from short exposures), and its slope is the PM. The quoted errors are formal values of the fit (see text for a discussion of the actual uncertainties). The lower panel shows the residuals to each fit.

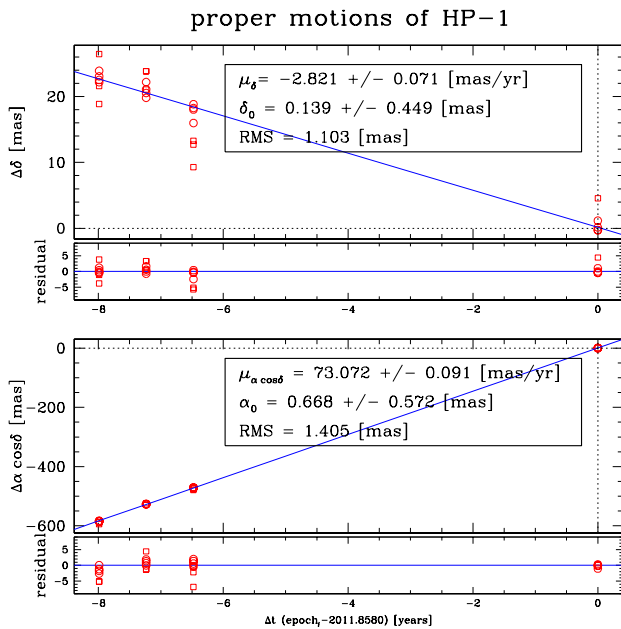


Figure 7. Same as in Fig. 6 but for HP-1.

indicate the corrections to be applied to our reference-frame positions at epoch 2011.858. However, these small corrections make sense only in relative terms, the uncertainties in the absolute positions being dominated by the uncertainties in the 2MASS absolute zero points. The lower panels in each half of Fig. 6 show the residuals to the fit, and the RMS of these residuals is labelled.

We attempted an analogous fit to all of the sources in the master frame. As an example of these, Fig. 7 shows our derived PMs for another object of interest in the field, the high-PM source HP-1 (K09). It is interesting to note that spectra of HP-1 suggest it is a late-M star, at a maximum distance of 500 pc (i.e., neglecting interstellar extinction); therefore, the geometric parallax should show a deviation from the linear fit of at least 2 mas.

It is worth mentioning that our derived PMs are consistent with those found by K13 (for the objects in common), although with much higher precision given our increased time baseline.

In the left panel of Fig. 8 we show the vector-point diagram (VPD) for the 872 objects (out of 1148) in the reference frame for which it was possible to derive relative proper motions. The adopted zero point of the motion is indicated by dotted lines. For 222 of them (indicated in black with their error ellipses), four epochs were employed, while for 296 (indicated in blue), just three epochs. Objects having uncertainties larger than 0.25 mas yr^{-1} are indicated with crosses. For reference, a red circle at $(75, 45) \text{ mas yr}^{-1}$ indicates the 0.25 mas yr^{-1} uncertainties. For 354 objects there are only two epochs (magenta). Two arrows indicate the motions of Tycho-G (red) and HP-1 (green). A close-up view of the VPD around the zero motion is shown Fig. 9. The right panel of Fig. 8 gives the spatial distribution of sources in the reference frame, for objects with four epochs (black), three epochs (blue), two epochs (magenta), and only one epoch (grey). Tycho-G is highlighted in red and HP-1 in green.

3.5.1 Uncertainties

The formal uncertainties provided by the weighted linear fit are probably much too optimistic, because our internal estimates of the errors within a given epoch (and based on multiple observations) could be severely underestimated. This is almost surely the case for the nondithered ACS/WFC epochs, where a portion of the systematic errors might cancel out and do not appear in the estimated internal errors.

But there is a more fundamental limitation. As mentioned at the beginning of Sec. 3, and more clearly stated at the end of Sec. 3.4, our PM accuracies are ultimately set by the PM dispersions of the set of stars with respect to which we have measured the relative positions — that is, the neighbouring stars used for the boresight corrections. A more realistic estimate of the errors is provided by Eq. 1, given at the end of Sec. 3.4, which requires the estimates of $\sigma_{\mu_{\alpha \cos \delta}}$ and $\sigma_{\mu_{\delta}}$.

To estimate these for each coordinate, we begin by taking the 68.27th percentile around the zero of the absolute value of the PMs obtained in the previous section (and shown in Fig. 8) as an initial guess of the PM dispersions (σ_{μ}). We then clipped at 3.5 times this value the objects with higher PMs, assuming them to be outliers. We then redetermined the dispersion of the PMs from the purged sample,

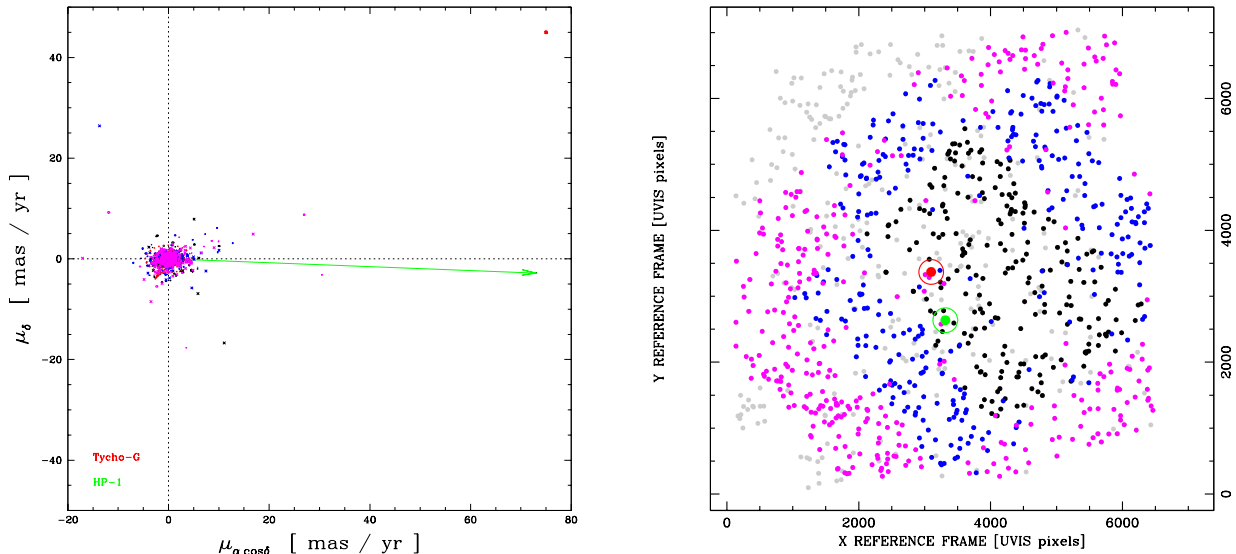


Figure 8. *Left:* Vector-point diagram for the 872 objects (out of 1148) in the reference frame for which it was possible to derive relative PMs. For 222 of them (indicated in black with their error ellipses) four epochs were employed, while for 296 (indicated in blue), three. For clarity, those with uncertainties larger than 0.25 mas yr^{-1} are indicated as crosses, and a red circle at position $(75;45) \text{ mas yr}^{-1}$ shows for reference the 0.25 mas yr^{-1} error. For 354 objects there are only 2 epochs (thin magenta points), and therefore no external estimates of the uncertainties were available; we simply combined in quadrature the RMS within each of the two epochs. Two arrows indicate the motion of Tycho-G (red) and HP-1 (green). The zero motion of the reference frame is indicated by dotted lines. A close-up view of the zero motion is shown Fig. 9. *Right:* Spatial distribution of sources in the reference frame having four epochs (black), three epochs (blue), two epochs (magenta), and only one epoch (grey). Tycho-G is highlighted in red and HP-1 in green.

again by taking the 68.27th percentile as a robust estimate of the PM dispersion (assumed as a first approximation to be Gaussian). We did this for both $\alpha \cos \delta$ and δ (using all PMs based on 4, 3, and 2 epochs), obtaining $\sigma_{\mu_{\alpha \cos \delta}} = 1.09 \text{ mas yr}^{-1}$ and $\sigma_{\delta} = 0.62 \text{ mas yr}^{-1}$. The larger dispersion in $\mu_{\alpha \cos \delta}$ than in μ_{δ} is caused by the almost exact alignment between α and the Galactic Plane at the location of Tycho-G.

Concerning the term N_{used} in Eq. 1, we took the average number of neighbouring stars used to compute the boresight correction in the adopted frames: $N_{\text{used}} = 39$. Therefore, a more realistic estimate for the expected uncertainties in our PMs is $(\overline{\sigma_{\mu_{\alpha \cos \delta}}}; \overline{\sigma_{\mu_{\delta}}}) = (\sigma_{\mu_{\alpha \cos \delta}}/\sqrt{39-1}; \sigma_{\mu_{\delta}}/\sqrt{39-1}) = (0.18; 0.10) \text{ mas yr}^{-1}$. Thus, our estimated relative proper motion for Tycho-G is

$$(\mu_{\alpha \cos \delta}; \mu_{\delta})_{J2000.0} =$$

$$(-2.63; -3.98) \pm (0.06; 0.04) \pm (0.18; 0.10) \text{ mas yr}^{-1},$$

where the first terms in the uncertainties are the formal errors, which are negligible relative to the expected errors given by the second term. It is worth noting that these values for Tycho-G are consistent with those recently obtained by K13, although at a much higher accuracy than those of K13, thanks to our larger time baseline.

To reiterate, the dominant uncertainties take into account that all of our measurements of positions and PMs of the target stars are relative to the average motions of the bulk of the other stars in the field, and specifically to the stars used to compute the boresight corrections. Note that

even had we measured the relative positions of our sources (within each epoch) with infinite precision, this dominant “kinematic component” to the error budget would still remain, as our positions are measured with respect to an ensemble of objects which are actually *not* fixed.

We conclude this section by noting that the residuals to the fit, shown in the bottom panels of Figs. 6 and 7, are caused by unaccounted sources of error, but in principle could also reflect the geometric parallaxes (of course *relative* parallaxes and not absolute parallaxes, as for all the other measurements in this work). Although theoretically possible, we have not attempted here to solve for two positions (α_0, δ_0) , two proper motions $(\mu_{\alpha \cos \delta}, \mu_{\delta})$, and the parallax (π) with just 6 independent data points [(4-1) epochs \times 2 coordinates].

4 THE NI ABUNDANCE OF TYCHO-G REVISITED

The Ni abundance of Tycho-G was first determined as $[\text{Ni}/\text{Fe}] = 0.16 \pm 0.04$, using a high-resolution Keck-I/HIRES spectrum (GH09). Recently, K13 reanalysed the same spectrum and derived $[\text{Ni}/\text{Fe}] = 0.07 \pm 0.04$. They argue that this difference could be explained by differences in equivalent width (EW) measurements of Ni lines which may be related to continuum normalisation and/or local continuum placement.

We have now revised the Ni abundance found by GH09 using automatic tools able to search for and fit the contin-

uum, and to measure the EWs of Ni lines in the HIRES spectrum of Tycho-G. We use the code ARES (Sousa et al. 2007) and the Ni line list from GH09, which comes from the abundance analysis of Gilli et al. (2006). Within the ARES code we choose the value 0.965 for the “rejt” parameter to take into account the relatively low S/N (~ 30) of the HIRES spectrum. After running ARES, we also filter the output line list, requiring the Gaussian FWHM of the output fitted Ni lines to be in the range 0.08–0.25 Å in order to avoid wrong fits. The instrumental broadening of this spectrum is about 0.14 Å at $\lambda = 6000$ Å, but we allow this range because of the relatively low S/N.

K13 estimate the average uncertainty in the EW determination to be 6.5 mÅ. We thus decided to remove all weak lines with EWs below 15 mÅ, to avoid uncertain measurements. We also apply a very restrictive 1.5σ clipping in the Ni abundance values to discard the possible outliers. The final result including 12 Ni lines gives $A(\text{Ni}) = \log[N(\text{Ni})/N(\text{H})] + 12 = 6.28$ ($\sigma = 0.11$, $\Delta_\sigma = 0.03$), where σ is the dispersion of the Ni abundance from N lines and $\Delta_\sigma = \sigma/\sqrt{N}$.

We now want to compare the Ni abundance of Tycho-G with high-quality abundance data from stars observed with the HARPS spectrograph on the 3.6-m telescope at La Silla Observatory (Neves et al. 2009).

We cross-check our line list with the Ni line list of Neves et al. (2009) and find 8 lines in common. The derived Ni abundance is $A(\text{Ni}) = 6.30$ ($\sigma = 0.13$, $\Delta_\sigma = 0.05$, $N = 8$) according to this new line list. We measured the EWs of these 8 Ni lines in the Kurucz solar ATLAS (Kurucz et al. 1984) to derive the solar Ni abundance and obtained $A(\text{Ni})_\odot = 6.25 \pm 0.00$, which we use to determine the $[\text{Ni}/\text{Fe}] \equiv \log[N(\text{Ni})/N(\text{Fe})] - \log[N(\text{Ni})/N(\text{Fe})]_\odot$ ratio. Therefore, taking into account the metallicity of Tycho-G, $[\text{Fe}/\text{H}] = -0.05$, our revised Ni abundance is $[\text{Ni}/\text{Fe}] = 0.10 \pm 0.05$.³ This revised Ni abundance is between the values given by GH09 and K13, but is consistent within the error bars with both values. We think that this value may be more accurate than that of GH09, since it was obtained using automatic tools which may be more appropriate when dealing with low-S/N spectra.

In Fig. 10 we compare the $[\text{Ni}/\text{Fe}]$ abundance ratio of Tycho-G with those of F-, G-, and K-type stars in the solar neighbourhood from Neves et al. (2009), which obviously were measured with the same line list and thus the same $\log gf$ values. We have corrected one of the points at $[\text{Ni}/\text{Fe}] = 0.18$ and $[\text{Fe}/\text{H}] = 0.03$ in Neves et al. (2009), which shows an unexpectedly high abundance dispersion, by removing the Ni abundance outliers from some spectral Ni lines using a 1.5σ clipping procedure (see González Hernández et al. 2013). This gives a revised value for this star, HD 209458, of $[\text{Ni}/\text{Fe}] = -0.03$. The average value of

³ Note that the uncertainty (0.05) has slightly increased compared with previous work by GH09 (0.04), mostly because of abundance dispersion (since other sources of error cancel out when computing the abundance ratio $[\text{Fe}/\text{Ni}]$). Also, we now use updated oscillator strengths, and we compare our derived abundance with a new high-quality set of abundances. The reference Galactic trend (Neves et al. 2009) appears to be slightly higher than before (Gilli et al. 2006), probably due to the different choice of Ni lines and different oscillator-strength values.

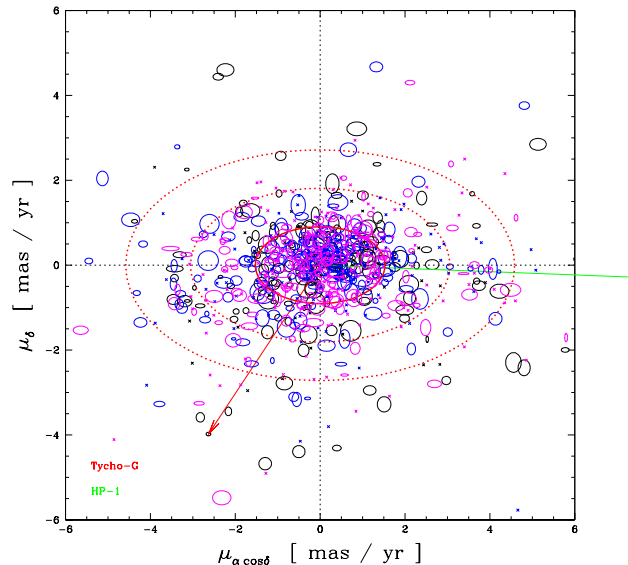


Figure 9. Close-up view of the left panel in Fig. 8 around the zero motion of the reference frame. The ellipse in red, with semi-axes $\sigma_{\mu_\alpha \cos \delta} = 1.38 \text{ mas yr}^{-1}$ and $\sigma_\delta = 0.83 \text{ mas yr}^{-1}$, shows the assumed PM distribution of objects in the field. For reference, $2\times$ and $3\times$ larger semi-axes are shown with dotted lines. Clearly, Tycho-G has significantly different PMs compared with the bulk of stars in the field.

the $[\text{Ni}/\text{Fe}]$ ratio in the relevant range of metallicities (i.e., $[\text{Fe}/\text{H}] = -0.05 \pm 0.09$) in thin-disk and thick-disk stars of the sample in Neves et al. (2009) is 0.00 ± 0.03 ($N_{\text{stars}} = 129$) for thin-disk F-, G-, and K-type stars, and 0.01 ± 0.03 ($N_{\text{stars}} = 7$) for thick-disk F-, G-, and K-type stars. The average value for solar analogs in González Hernández et al. (2010, 2013) is -0.02 ± 0.03 ($N_{\text{stars}} = 24$). The Ni abundance in Tycho-G, taking into account all known uncertainties, still appears to be slightly above (at almost 1.7σ) the Galactic trend, mostly defined by main-sequence stars in the solar neighbourhood (see Fig. 10). Error bars are relatively large as a result of the modest quality of the spectrum of this very faint star, despite hours of integration time with the 10-m Keck I telescope.

5 THE ORBIT OF THE BINARY PRECURSOR OF SN 1572

The PM measured for Tycho-G can be translated into a tangential motion (i.e., perpendicular to the line of sight) once the distance to the object is known. Its distance lies in the range $2.48 \pm 0.21 \text{ kpc}$ to $4.95 \pm 0.52 \text{ kpc}$ (GH09), which encompasses the estimated distance to the SNR ($2.83 \pm 0.79 \text{ kpc}$; Ruiz-Lapuente 2004). We will assume, in the following, that Tycho-G is indeed inside the SNR, to derive its tangential motion.

The PM parallel to the celestial equator, $\mu_{\alpha \cos \delta} = -2.63 \pm 0.18 \text{ mas yr}^{-1}$, translates into $v_\alpha = -35 \pm 10 \text{ km s}^{-1}$, while $\mu_\delta = -3.98 \pm 0.10 \text{ mas yr}^{-1}$ gives $v_\delta = -53 \pm 14 \text{ km s}^{-1}$, where the uncertainties come almost entirely from

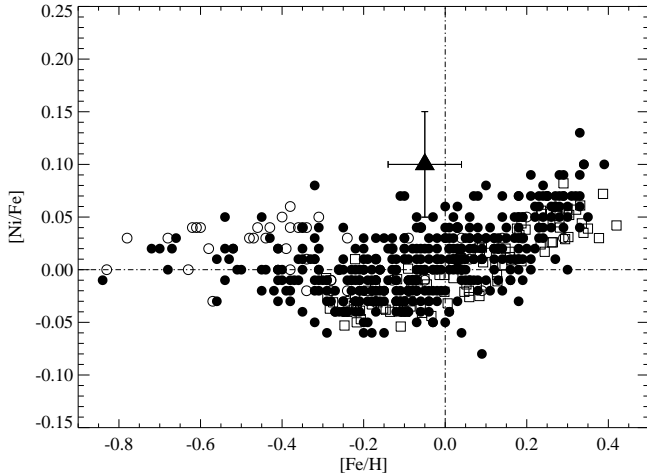


Figure 10. $[\text{Ni}/\text{Fe}]$ abundance ratio of Tycho-G (filled triangle) in comparison with the abundances of F-, G-, and K-type metal-rich dwarf stars (Neves et al. 2009). Thin-disk stars are depicted as filled circles, whereas transition and thick-disk stars are the empty circles. Solar analogs are shown as empty squares (González Hernández et al. 2010, 2013). The size of the error bars indicates the 1σ uncertainty. The dashed-dotted lines indicate solar abundance values.

those in the distance. The total tangential velocity is thus $v_t = \sqrt{v_\alpha^2 + v_\delta^2} = 64 \pm 11 \text{ km s}^{-1}$. Since the radial velocity of Tycho-G is $v_r = -80 \pm 0.5 \text{ km s}^{-1}$ (GH09), its total velocity (referred to the Local Standard of Rest) is, in absolute value, $v_{\text{tot}} = \sqrt{v_t^2 + v_r^2} = 102 \pm 9 \text{ km s}^{-1}$.

We could interpret the total velocity of the star as corresponding to that of its orbital motion and arising from disruption of the binary orbit because of the explosion of the WD component of the system. The average tangential velocity of disk stars at the position and distance of the SNR is negligible compared with that measured for star G. However, since the average radial velocity in the direction of Tycho’s SNR, at a distance $d \approx 2.8 \text{ kpc}$ from the Sun, is $\langle v_r \rangle \approx -37 \pm 20 \text{ km s}^{-1}$ (from the Besançon model of the Galaxy; Robin et al. 2003), it would be more appropriate to take as the peculiar radial velocity due to the orbital motion $v_r \approx -43 \pm 20 \text{ km s}^{-1}$. Thus, the total orbital velocity would become only $v_{\text{orb}} = 77 \pm 16 \text{ km s}^{-1}$. If Tycho-G were actually inside the SNR, its radial velocity would thus be slightly more than 2σ above average. Nevertheless, in assessing the peculiarity of the kinematics of Tycho-G (which will be done in the next section), the uncertainty in its distance must be taken into account. Based on the same reference, the radial velocity would be between 2.2σ (lower limit on the distance; star in the foreground of the SNR) and 1.2σ (upper limit; star in the background) above the average. Note that the ratio of v_t to v_r gives the inclination of the plane of the orbit with respect to the line of sight, and hence determines the projection of the rotational velocity along that line assuming coplanarity ($i \approx 34^\circ$).

Adopting $1.4 M_\odot$ and $1 M_\odot$ as the respective masses of the WD and its companion at the time of the explosion, we obtain an orbital separation of $a = (26 \pm 12) R_\odot$ and a period of $P = 10 \pm 7 \text{ days}$. Applying Eggleton’s (1983) formula for the effective Roche-lobe radius of the companion star, we

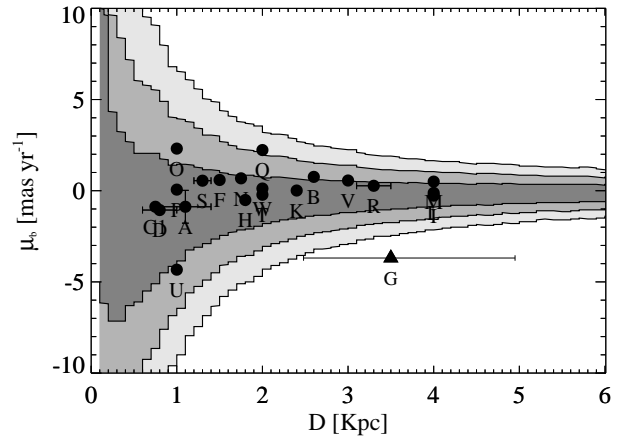


Figure 11. The distribution of proper motions μ_b , perpendicular to the Galactic plane, as a function of distance, in the direction of the X-ray centroid of Tycho’s SNR, for thin-disk and thick-disk stars together (and $[\text{Fe}/\text{H}] > -0.14$), according to the Besançon model of the Galaxy (Robin et al. 2003). 1σ , 2σ , and 3σ regions are indicated. The position of Tycho-G is depicted as a triangle, $D[\text{kpc}] = 3.50^{+1.45}_{-1.02}$ and $\mu_b[\text{mas yr}^{-1}] = -3.69 \pm 0.10(0.04)$. The range of distances to Tycho-G, as well as the PM measured in this work, are indicated by the horizontal line. The lengths of the vertical segments at the two ends of the line correspond to the error bar of the PM measurement. The positions of all the other stars discussed in Section 9 (see also Table 3), and with estimated distances $D \leq 6 \text{ kpc}$, are also shown. The error bars in μ_b are smaller than the sizes of the points.

have $R_L = (9 \pm 4) R_\odot$. This means that if Tycho-G was indeed the companion of the SN, at the time its radius was considerably larger than its present radius, which is within the range $R \approx 1\text{--}2 R_\odot$ (GH09).

6 THE KINEMATICS OF TYCHO-G AND IMPLICATIONS

With the present high-precision results in its proper motion, the kinematics of Tycho-G can now be reevaluated. The new measurements have confirmed a high proper motion perpendicular to the Galactic plane. As already mentioned in Section 1, a similar result is obtained by K13. If the star were at the distance of Tycho’s SNR (taken here to be 2.83 kpc), its velocity would be $v_b = -51 \pm 1.5 \text{ km s}^{-1}$. Let us now separately consider the probability, for Tycho-G, of being either a random thin-disk, thick-disk, or halo star.

Thin disk. The metallicity and height above the Galactic plane of Tycho-G are typical of a thin-disk star. Taking again the Besançon model of the Galaxy (Robin et al. 2003) as an approximation to the kinematic structure, the average for all disk stars (thin and thick disk together) having $[\text{Fe}/\text{H}] > -0.14$, at the Galactic latitude of the remnant and at its distance, is only $\langle v_b \rangle = -2.6 \pm 12 \text{ km s}^{-1}$ (see Fig. 11). Thus, the velocity of Tycho-G is almost 4σ above the average, and the probability of its being due to chance alone should be $P \lesssim 10^{-4}$. Given the limits on the distance to Tycho-G quoted in the preceding section, we find that v_b must, in any case, be within the range $-45 \pm 1 \text{ km s}^{-1}$ to

$-90 \pm 3 \text{ km s}^{-1}$. For the shortest possible distance (2.48 kpc), v_b would still be $\sim 3.7 \sigma$ above average. If Tycho-G were in the background of the SNR, then at the upper limit of its distance (4.95 kpc), v_b would climb to 7.5σ . For the shortest distance, as stated in the previous section, the radial velocity would be 2.2σ above average (taking the same model as a reference). While the metallicity of Tycho-G ($[\text{Fe}/\text{H}] = -0.05 \pm 0.09$) is typical of a thin-disk star, $[\text{Ni}/\text{Fe}]$ is almost 1.7σ above the Galactic trend ($P \lesssim 0.1$), and thus the total probability of finding, at random and in a single try, a thin-disk star with such a high velocity perpendicular to the Galactic plane and $[\text{Ni}/\text{Fe}]$ excess together, would be the product of the two probabilities, which gives $P \lesssim 10^{-5}$ (at the assumed distance of the SNR), and at most $P \lesssim 10^{-4}$ (this value corresponding to the shortest possible distance).

Thick disk. GH09 (see their Fig. 10, and also Fuhrmann 2005) have shown that there are some thick-disk stars, even within the metallicity range of Tycho-G, having kinematics apparently similar to that of this star (although v_b is not shown directly in the Toomre diagram, but only the combination $(U^2 + W^2)^{1/2}$). However, at the location of Tycho's SNR, the density of thick-disk stars with metallicities higher than the above limit is much lower than that of thin-disk stars (in the model of reference, the fractional density of the total of the thick-disk stars is only 3.4%; see Table 2 of Robin et al. 2003). Since thick-disk stars appear as the closest relatives of Tycho-G, we will discuss this case more in detail.

The relative number density of thick-disk stars close to the Galactic plane is somewhat uncertain: Robin et al. (1999) and Buser et al. (1999) found values around 6%, while Binney & Tremaine (2008) adopt a value as low as 2%. Concerning metallicity, although the average metallicity of thick-disk stars is lower than that of thin-disk stars, there is, nonetheless, some overlap. However, the fraction of thick-disk stars with metallicities $[\text{Fe}/\text{H}] > -0.14$ is very small. In the same Fig. 10 of GH09, for instance, a sample of 38 thick-disk stars reduces to only 6 when the metallicity constraint is applied. This would mean that such stars (taking 6% as the fractional density of thick-disk stars) constitute only $\sim 0.9\%$ of the number density in the region where Tycho-G is found. In a volume-complete sample of thin-disk and thick-disk stars in the solar neighbourhood (a total of 271 F-, G-, and K-type stars), Fuhrmann (2011, Fig. 15) finds only 2 thick-disk stars in the metallicity range of Tycho-G, giving a relative number density of $\sim 0.7\%$ for these “transition stars.” However, as we show in Figure 12, the number of stars in the sample that have metallicities within the range of that of Tycho-G is only 128, so the relative number density of “transition stars” in that range becomes $\sim 1.5\%$.

If we were to adopt $\sigma_W = 39 \pm 4 \text{ km s}^{-1}$ (Bensby et al. 2003) for the velocity dispersion of thick-disk stars perpendicular to the Galactic plane, we would find v_b of Tycho-G (at the distance of the SNR) to be 1.28σ above the average thick-disk stars ($P \lesssim 0.2$). Multiplying by the probability of finding, at random, a thick-disk star with a metallicity as high as that of Tycho-G, 0.015, as we have just seen, we would have $P \lesssim 0.003$. However, the dispersion in v_b of the thick-disk stars with metallicities as high as that of Tycho-G is smaller. Using again the Besançon model of the Galaxy, we find that for those stars with a velocity dispersion

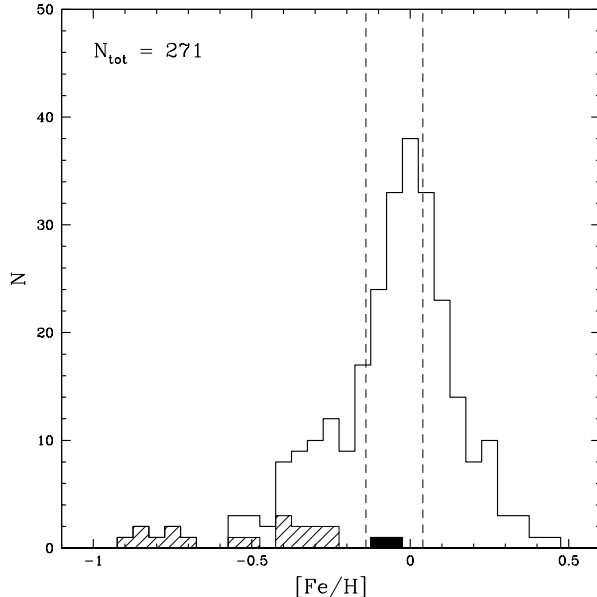


Figure 12. Metallicity distribution function of a volume-complete sample of nearby F, G, and K stars belonging to the Galactic disk. Shaded histogram corresponds to the thick-disk stars. Vertical dashed lines mark the metallicity range of Tycho-G. Highlighted in black are the only two thick-disk stars with metallicities within that range. The total sample comprises 271 stars, and the number of stars within the said range is 128 (adapted from Fuhrmann 2011).

of only $\sigma_W \simeq 20 \pm 2 \text{ km s}^{-1}$ (intermediate between that of the bulk of thick- and thin-disk stars), the v_b of Tycho-G would be slightly above 2.5σ ($P \lesssim 0.012$) if it were at the distance of the SNR. For the nearest possible distance, since then v_b is only -45 km s^{-1} , it would be at 2.25σ ($P \lesssim 0.024$), and for the largest distance ($v_b = -90 \text{ km s}^{-1}$), it would be at 4.5σ . Therefore, the probability of finding, at random, a thick-disk star with a metallicity above the lower limit for that of Tycho-G, and moving at least as fast, within the range of possible its distances, becomes $P \lesssim 3.7 \times 10^{-4}$ at most (star at a distance of only 2.48 kpc).

In the preceding discussion, we have not yet taken into account any Ni overabundance. We see from Section 4 that the Ni abundance ratio $[\text{Ni}/\text{Fe}] = 0.10 \pm 0.05$ is 1.3σ above the Galactic trend for thick-disk stars ($P \lesssim 0.2$), and the same reasoning as for thin-disk stars applies: the probability of finding by chance a thick-disk star with a metallicity as high as that of Tycho-G, and with its kinematics and Ni overabundance, in a single try, is $P \lesssim 7.4 \times 10^{-5}$ (i.e., less than 1 in ~ 13500).

Halo. Although the value of v_b for Tycho-G falls within the velocity dispersion for halo stars (85 km s^{-1} , according to Robin et al. 2003), the possibility that it belongs to such a population can be almost completely excluded. Not only is the number density of halo stars at the position and range of distances of Tycho-G $\sim 10^{-3}$ times the local density, but for those stars $[\text{Fe}/\text{H}] = -1.5 \pm 0.5$ (Gilmore & Wyse 1985), which means that the metallicity of Tycho-G ($[\text{Fe}/\text{H}] = -0.05 \pm 0.09$) is almost 3σ above the average. The prob-

ability of finding such a star at random is thus $P \lesssim 3 \times 10^{-6}$ (combining metallicity and relative star density).

If Tycho-G were just a chance interloper, it would most likely be a thick-disk star. As we have seen, this means having picked a star, unrelated to the SNR but within its distance range and in a small area around its centre, of which there are fewer than 1 in ~ 13500 . However, as discussed in Section 9, there are four other stars, apart from Tycho-G, at distances at least marginally compatible with that of the SNR and inside the explored area of the sky, which would increase the probability by a factor of 5 ($P \lesssim 3.7 \times 10^{-4}$).

The low rotational velocity of Tycho-G ($v_{\text{rot}} \sin i \lesssim 6.6$ km s $^{-1}$; see GH09) is well explained even if we assume that the rotational period P_{rot} has remained unchanged after the explosion and that it was $P_{\text{rot}} = P_{\text{orb}}$ (synchronous rotation). From GH09, the current radius of the star must be $R \approx 1\text{--}2 R_{\odot}$. With a period $P_{\text{rot}} \approx 10$ days (from the preceding section), and for the larger radius, $v_{\text{rot}} \approx 10$ km s $^{-1}$; with $i \approx 34^{\circ}$ (the value obtained from our reconstruction of the orbit, Section 5), $v_{\text{rot}} \sin i \approx 5.6$ km s $^{-1}$, a small value. The effects of the impact of the SN ejecta on the companion studied by Pan et al. (2012a) and Liu et al. (2013) would reduce v_{rot} even more. Concerning this last point, it should be noted that the hydrodynamic simulations have been done only for main-sequence companions, and that the removal of angular momentum from less compact stars should be larger.

In conclusion, there is a very low probability ($P \lesssim 0.00037$) for a star with the kinematics, metallicity, and Ni excess of Tycho-G, and within the distance range of Tycho's SNR, to have been found by chance when exploring the central region of the remnant.

7 THE POSITION OF TYCHO-G

The position of Tycho-G is within the uncertainties pertaining to the location of the site of the explosion inside SNRs. In the case of Tycho, the centroids of the X-ray emission determined from the *Chandra X-ray Observatory* images (Warren et al. 2005) and from *ROSAT* (Hughes 2000) differ by only $6.5''$, but they are $\sim 26\text{--}28''$ away from the centroid of the radio emission, determined from VLA observations (Reynoso et al. 1997). The current position of Tycho-G (see Table 2) is at an angular distance of $29.8''$ from the *Chandra* X-ray centroid ($\alpha_{\text{J2000.0}} = 00^{\text{h}}25^{\text{m}}19.40^{\text{s}}$, $\delta_{\text{J2000.0}} = +64^{\circ}08'13.98''$), which amounts to $\sim 10\%$ of the radius of Tycho's SNR. From the PM obtained in Section 3, the position of the star in 1572 was $\alpha_{\text{J2000.0}} = 00^{\text{h}}25^{\text{m}}23.75^{\text{s}}$, $\delta_{\text{J2000.0}} = +64^{\circ}08'03.73''$, and its angular distance with respect to the same centroid should thus have been similar, $30.3''$.

Asymmetries can arise from interaction of the SNR with the ambient medium, but they can also be intrinsic to the SN ejecta (and, of course, both can occur simultaneously). In Tycho, there is evidence that the ejecta encountered a dense H cloud at the eastern edge, giving rise to brighter emission and lower velocity there (Decourchelle et al. 2001), which would place the site of the explosion to the E of the centroid of the SNR. More recently, Williams et al. (2013), from mid-infrared observations of dust emission, find an overall

gradient in the ambient density, with densities being higher in the NE than in the SW. From two-dimensional hydrodynamic simulations, they find that an overall round shape of the SNR is produced, but that the centre of the explosion is then offset from the geometric centre by $\sim 10\%$ in the direction of the higher ambient density (that is, toward the NE). At the same time, they favor a distance of 3–4 kpc to the SNR. The second kind of asymmetry (intrinsic) has been found by Winkler et al. (2005) in the remnant of SN 1006, another SN Ia. The projection of the remnant on the plane of the sky looks quite round, as in the case of Tycho, but observations of background UV sources show that the Fe-rich ejecta are egg-shaped, and elongated at an angle with the line of sight; see Figure 8 of Winkler et al. (2005), and also their Figure 1 for the projection on the plane of the sky. This work has recently been extended to the distribution of the O-burning and incomplete Si-burning products (Si, S, and Ar) by Uchida et al. (2013), who deduce a velocity asymmetry of ~ 3100 km s $^{-1}$. Winkler et al. (2005) concluded that the position on the sky of the site of the explosion differs from the X-ray centroid by as much as $\sim 20\%$ of the radius of the SNR. Kerzendorf et al. (2012) have objected that the models of asymmetric SN Ia explosions by Maeda et al. (2010) confine the asymmetry to the distribution of the innermost ejecta, while the outer ejecta show spherical symmetry, and that the position of the centre of the WD, at the time of the explosion, should rather be given by the centroid of the outer ejecta. However, in those models, a velocity offset of the inner ejecta (with respect to the original centre of the star) is attributed to the deflagration phase of the explosion, while the more spherically symmetric mass ejection is produced by the transition from deflagration to detonation, closer to the surface. It is hard to imagine that while the inner layers are moving away from the original centre, the centroid of the outer layers remains anchored in that position. Thus, in this type of asymmetric explosion, neither the present centroid of the Fe-rich ejecta nor that of the outer ejecta should correspond to the position of the centre of the WD at the time of the explosion. No similar analysis has been done for SN 1572, but the spectrum of its light echo suggests that the explosion was also aspherical (Krause et al. 2008).

Among the stars with $m_V \leq 22$ mag, the closest one to the *Chandra* X-ray centroid is Tycho-B (see Fig. 13, and Tables 2 and 3). In order of increasing distance are stars Tycho-A, -C, -E, -D, -F, -J, and then -G. As discussed in Section 9, none of these other stars shows any sign of being related to the SN explosion.

8 THE LUMINOSITY OF TYCHO-G

The luminosity of Tycho-G is within the range $1.9 < L_*/L_{\odot} < 7.6$, as calculated from its effective temperature and surface gravity (assuming a mass of $1 M_{\odot}$; GH09). What should be expected for the companion of a SN as recent as SN 1572?

Podsiadlowski (2003) calculated the luminosity evolution of a subgiant star of $1 M_{\odot}$, $R_* = 2.5 R_{\odot}$, and $L_* \approx 3 L_{\odot}$, after being hit by the ejecta of a SN Ia. He assumed that $0.2 M_{\odot}$ were removed by the impact (based on the hydrodynamic calculations of Marietta et al. 2000),

and that variable amounts of energy were deposited uniformly in the outermost 90% of the radial extent of the remaining object (containing $0.57 M_{\odot}$). Such amounts ranged from 4×10^{47} erg (close to the energy needed to unbind those layers completely) down to zero. He found, in all cases, that the luminosity evolution was initially much faster than the Kelvin-Helmholtz time scale of the presupernova subgiant, since it was determined by the thermal time scale of the outer layers of the star, which is many orders of magnitude shorter. Depending on the amount of energy deposited, the luminosity of the companion, 440 yr after the SN explosion, might range from $\sim 200 L_{\odot}$ to $\sim 0.1 L_{\odot}$ (see Fig. 2 in Podsiadlowski 2003). The result also depends strongly on the mass of the star at the time of the explosion and on the amount of mass removed by the explosion (which, in turn, depends on the evolutionary stage of the subgiant).

Recently, Shappee et al. (2013) have calculated the post-explosion evolution of a main-sequence companion of $1 M_{\odot}$. From the hydrodynamic simulations of Pan et al. (2012a), which show that in this case most ($\sim 65\%$) of the mass lost from the impact of the ejecta is due to ablation (heating by the shock front) and the rest ($\sim 35\%$) is removed by stripping (momentum transfer by the shock), they construct an initial model by heating the whole star until it generates a stellar wind able to expel the same amount of mass that is lost by ablation in the hydrodynamic calculation. They then follow the evolution of the star by means of a standard one-dimensional code, finding that after ~ 500 yr, the luminosity of the companion should still be $\geq 20 L_{\odot}$, while $T_{\text{eff}} \leq 5500$ K. Note that their pre-explosion model has a radius $R \approx 1 R_{\odot}$, significantly smaller than that inferred in Section 5 for Tycho-G at the same stage under the assumption that it was the companion of SN 1572.

Pan et al. (2012b), based on their own hydrodynamic models (Pan et al. 2012a), find that the evolution of the remnant star strongly depends not only on the amount of energy absorbed from the explosion, but also on the depth of the energy deposition. They calculate the evolution of several pre-explosion models through the hydrodynamic and hydrostatic stages. One of them (their model E), 440 yr after the explosion, is the closest in mass, radius, and effective temperature to Tycho-G, having a luminosity higher than that of Tycho-G by only a factor of two. Again, however, the initial model is more compact than Tycho-G should have been at the time of the explosion. As it can be seen from the hydrodynamic simulations of Marietta et al. (2000), the less compact the star is, the more mass is removed by stripping and less by ablation, which also means less energy deposited into the layers that remain bound.

We stress once again that the calculations that predict, for a stellar SN Ia companion 440 yr after the explosion, luminosities higher than that of Tycho-G, have all been made for main-sequence stars, and that the outcomes might be significantly different for even slightly more evolved ones (a point that also affects rotation, as indicated in Section 6). The reconstruction of an evolutionary scenario, leading to a pre-explosion configuration similar to the one deduced in Section 5, should include nonconservative mass transfer and the different evolution of the orbital separation before and after inversion of the mass ratio between the two stars. We also note that, depending on the amount of mass lost from the impact of the SN ejecta, on the amount of energy

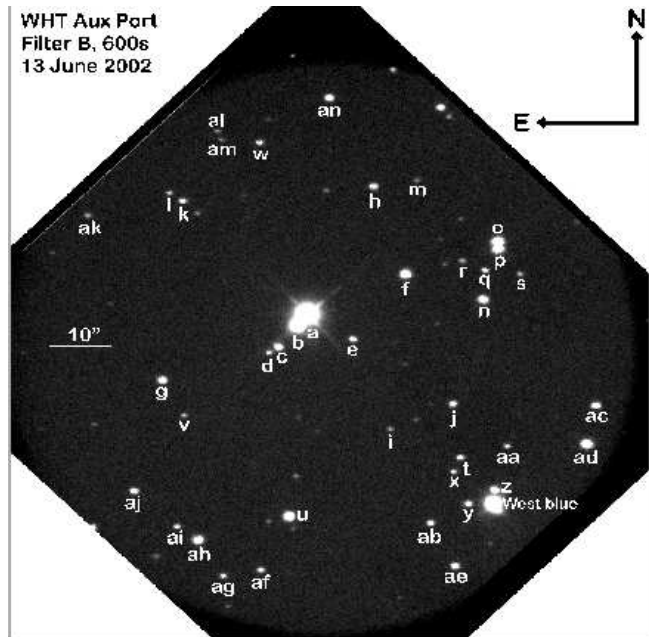


Figure 13. *B*-band image taken with the 4.2-m William Herschel telescope, showing all of the named stars near the centre of Tycho's SNR.

injected, and on how that energy is distributed inside the remaining star, the object might not have reached thermal equilibrium yet; it could be slowly expanding on a Kelvin-Helmoltz time scale, obtaining energy for this from internal sources, as suggested by Podsiadlowski (2003).

9 OTHER STARS AROUND THE CENTRE OF TYCHO'S SNR

In RL04, radial velocities were measured and distances estimated for 13 stars (including Tycho-G) located within an angular distance of $39''$ from the centroid of the X-ray emission of Tycho's SNR and with $V < 22$ mag, as well as for 3 slightly more distant stars, up to $41.5''$ from the same point and also brighter than the said magnitude (Tables 1 and S3 of RL04). Although PMs measured with WFPC2 aboard *HST* were graphically displayed in Figure 1 of RL04, they were numerically given only for Tycho-G. Now, with the much more precise PMs in Table 2 of the present paper, and with new estimates of the distances for some of those stars, we can rediscuss the kinematics of the sample and the possible association of each of its members with SN 1572. In Table 3 we give *BVR* photometry, estimated distances, and velocities v_{α} (parallel to the celestial equator) and v_{δ} (perpendicular to it) for the full set of 24 stars located within $42''$ from the X-ray centroid (see Fig.13 for labels and positions) and brighter than $V = 22$ mag. We briefly comment on each of them next.

Tycho-A is a giant star, at a distance between 1.1 ± 0.3 kpc (RL04) and 1.4 ± 0.8 kpc (K13), thus closer than Tycho's SNR. Its radial velocity v_r (referred to the Local Standard of Rest, LSR) is between -23 and -28.5 km s^{-1} . Owing to saturation even in the *HST*/WFC3/UVIS short images, no PM has been measured in the present work; however,

K13 (who use 0.5 s ACS/WFC exposures to derive their master frame) give $\mu_{\alpha\cos\delta} = -0.09 \pm 1.17$ mas yr⁻¹ and $\mu_{\delta} = -0.89 \pm 0.90$ mas yr⁻¹, which translate into $v_{\alpha} = -0.5 \pm 3$ km s⁻¹ and $v_{\delta} = -4.6 \pm 5$ km s⁻¹ assuming the RL04 distance. The radial velocity is thus consistent with the distance for a star belonging to the Galactic thin disk, and the small total tangential velocity is also typical of such a stellar population.

Tycho-B is a main-sequence star of spectral type A8–A9, at a distance between 2.6 ± 0.5 kpc (RL04) and 1.8 ± 0.8 kpc (K13). Its radial velocity is between -38 and -44.5 km s⁻¹, indicating that Tycho-B is a thin-disk object, like Tycho-A; its higher radial velocity corresponds to the larger distance. The components of the tangential velocity, calculated from the PMs in Table 2 ($v_{\alpha} \approx -21$ km s⁻¹, $v_{\delta} \approx 7$ km s⁻¹), are again typical of its population. It should be noted that the high rotational velocity measured by K13, $v_{\text{rot}} \sin i = 171_{-33}^{+16}$ km s⁻¹, is well within the range covered by stars of its spectral type (Abt & Morrell 1993, 1995). Thompson & Gould (2012) have attempted to relate Tycho-B to the SN, based on the low metallicity found by K13, by making it a member of a quadruple system: one binary pair giving a double WD system that produces the SN, plus another pair merging into a blue straggler (Tycho-B). The problem here is that the kinematics of Tycho-B very precisely match that of a thin-disk star.

Tycho-C corresponds to two different objects: a brighter, bluer star (C1) with $V = 19.06$ mag and $B - V = 2.00$ mag, and a fainter, redder one (C2) with $V = 20.53$ mag and $B - V = 2.38$ mag.

C1 appears to be a main-sequence star of spectral type K7 in the foreground of the SNR. It is at a distance of less than 1 kpc. Its radial velocity (-33 ± 6 km s⁻¹) was measured by RL04. Its PM (Table 2) gives the two components of its tangential velocity (Table 3) as $v_{\alpha} \approx -8$ km s⁻¹, $v_{\delta} \approx -0.4$ km s⁻¹, both of which are quite small. The star was classified by K13 as a red giant at $d = 5.5 \pm 3.5$ kpc, instead; however, from its colour, with a reddening $E(B - V) = 0.76$ mag (GH09) or $E(B - V) = 0.86$ mag (estimated by K13 for Tycho-B, at a much smaller distance), star C1 would be of spectral type K2, with $M_V \approx +0.2$ mag, and then its apparent magnitude would place it at an even larger distance, which is inconsistent with the small radial velocity.

C2 is probably a red-giant star in the background. No reliable measurement of v_r has been possible, but the PM was determined (Table 2). The combination of distance and PM makes it a member of the halo population.

Tycho-D is on the main sequence and has spectral type M1 (RL04; GH09). It is at a distance less than 1 kpc. No radial velocity could reliably be measured by RL04, but K13 give $v_r = -50.6 \pm 0.8$ km s⁻¹, which would be high for such a small distance (perhaps a hint of binarity). We see that both components of the tangential velocity are small ($v_{\alpha} \approx -8$ km s⁻¹, $v_{\delta} \approx -5$ km s⁻¹).

Tycho-E is a double-lined spectroscopic binary (GH09). Treated as a single star, it appears as a K2–K3 giant at a large distance, with $v_r = -26 \pm 18$ km s⁻¹ (RL04) or $v_r = -55.91 \pm 0.27$ km s⁻¹ (K13). The discrepancy is likely to come from the binarity, the star having been observed at different orbital phases in each of the two studies. The same might account for the claim by Ihara et al. (2007) that this star shows blueshifted iron absorption lines. For $d > 20$ kpc,

$v_{\alpha} \gtrsim -95$ km s⁻¹ and $v_{\delta} \gtrsim +27$ km s⁻¹, not particularly high for a star located at least ~ 0.5 kpc above the Galactic plane.

Tycho-F is on the main sequence, at spectral type F9 (GH09). From photometry, its distance should thus be ~ 1.5 kpc. The radial velocity is $v_r = -34 \pm 11$ km s⁻¹ (RL04). From its proper motion, both components of its tangential velocity are small ($v_{\alpha} \approx -23.5$ km s⁻¹, $v_{\delta} \approx 2$ km s⁻¹).

Tycho-G has been extensively discussed already. In Table 3 we show the two most extreme estimates of its distance (GH09) and the corresponding components of the tangential velocity.

Tycho-H, from its colour, could be either a giant of spectral type K0–K1 at a distance ~ 24 kpc, or a main-sequence star of the same spectral type at $d \approx 1.8$ kpc. Its radial velocity is $v_r = -71 \pm 10$ km s⁻¹, in better agreement with the longer distance. From the PMs, either $v_{\alpha} \approx -360$ km s⁻¹ and $v_{\delta} \approx -96$ km s⁻¹ (large distance), or $v_{\alpha} \approx -27$ km s⁻¹ and $v_{\delta} \approx 7$ km s⁻¹ (short distance). The star would belong to the halo in the first case and to the thin disk in the second one. For the short distance the radial velocity would be unusually high, but not the tangential velocity.

Tycho-I, from its colours (Table 3), could be either a K1–K2 main-sequence star at a distance ~ 4 kpc or a K6–K7 red giant at a very large distance. Its PMs have been determined (see Table 2), and we can thus calculate the components of its tangential velocity. In the first case, the tangential velocity would be small ($v_{\alpha} \approx 13$ km s⁻¹, $v_{\delta} \approx 4$ km s⁻¹).

Tycho-J is on the main sequence, with spectral type G8, at a distance ~ 9 kpc. Its radial velocity comes from RL04, and its PM gives, for the two components of its tangential velocity, $v_{\alpha} \approx -100$ km s⁻¹, $v_{\delta} \approx -12$ km s⁻¹.

Tycho-K could be either a G9–K0 giant or a G9 main-sequence star. In the first case, its distance would be ~ 27 kpc, and in the second case only ~ 2.4 kpc. Its radial velocity would fit well with the shorter distance. On the other hand, the PM is small, in better agreement with the longer distance.

Tycho-L, from the colours, should be of spectral type K0–K1 and could be, like the other stars in the sample for which only photometry is available, either on the main sequence or on the red-giant branch. In the former case, its distance would be ~ 4 kpc. In the second case, star L would be tens of kpc away. The components of the tangential velocity given in Table 3 ($v_{\alpha} \approx 7$ km s⁻¹, $v_{\delta} \approx 1.5$ km s⁻¹) are those corresponding to the shorter distance.

Tycho-M, from Table 3, could be either a main-sequence star of spectral type K2 or a red giant of the same type. In the first case, its distance would be ~ 4 kpc; thus, from the PMs in Table 2, the components of the tangential velocity would have the small values given in Table 3 ($v_{\alpha} \approx 12$ km s⁻¹, $v_{\delta} \approx 8$ km s⁻¹). If it were a red giant, it would be very far in the background.

Tycho-N is a main-sequence star of spectral type G0–G2, at a distance between 1.5 and 2 kpc. Its radial velocity comes from RL04. The kinematics are standard.

Tycho-O had its radial velocity measured by RL04. From its colour, it is a G5 main-sequence star, at $d < 1$ kpc. If it were instead a G5 giant, its distance would be ~ 7 kpc. In Table 3, the upper limits to the components of the tangential velocity are given for the shorter distance.

Tycho-P has a colour indicating a G2–G3 main-sequence star at a distance ~ 1 kpc. Were it a G4 giant, its distance would be ~ 8 kpc.

Tycho-Q is either a K3 main-sequence star at a distance ~ 2 kpc or a K2–K3 giant at a very large distance. v_α and v_δ in Table 3 are given for the former case.

Tycho-R is either a K2 main-sequence star at $d = 3.3 \pm 0.2$ kpc or, again, a very distant red giant of the same spectral type. As in previous cases, the tangential velocities are given only for the shorter distance.

Tycho-S is either a K8 main-sequence star at $d = 1.3 \pm 0.1$ kpc or a very distant M1 giant.

Tycho-T has an unknown radial velocity. From its colour, corresponding to K1, the distance could be either ~ 2 kpc if a main-sequence star or ~ 30 kpc if a red giant. In Table 3 we give the components of its tangential velocity only for the shorter distance.

Tycho-U has $v_r = -38 \pm 4$ km s $^{-1}$ (RL04). It is a G0 main-sequence star at a distance ~ 1 kpc. If it were a giant star, its distance would be > 8 kpc.

Tycho-V has no measured radial velocity. It appears to be a main-sequence star of spectral type K3–K4, at a distance ~ 3 kpc.

Tycho-W is a K3 main-sequence star at ~ 2 kpc.

From Table 3, we see that only four stars (B, K, R, and V), apart from Tycho-G, are at distances even marginally compatible with that of Tycho’s SNR. None of them shows the slightest kinematic peculiarity that might suggest any link with SN 1572. We also note that within this small sample of 23 stars, none shows velocities perpendicular to the Galactic plane comparable with that of Tycho-G, in full agreement with our previous discussion. Given the small number of stars in the central region of Tycho’s SNR, it is unlikely that one of them would show the unusual characteristics of Tycho-G without being related to the SN explosion.

10 SUMMARY AND CONCLUSIONS

A very accurate determination of the proper motions of 872 stars in the central region of Tycho’s SNR, based on images taken with *HST* in up to four different epochs and spanning a total of 8 years, has confirmed a high PM of Tycho-G perpendicular to the Galactic plane: $v_b = -50 \pm 14$ km s $^{-1}$. The probability of its being caused by chance alone is very small.

From the PM plus the radial velocity of Tycho-G, we have deduced the orbital separation, the orbital period, and the orientation of the plane of the orbit at the time of the explosion, if its present velocity comes from the orbital motion when Tycho’s SN exploded. We also derive the radius it should have had if it were then filling its Roche lobe. This radius is significantly larger than the current radius, and we speculate that the star might now be expanding on a thermal time scale.

We have also recalculated the Ni abundance of Tycho-G using the same high-resolution spectrum as in the previous work by GH09, but this time with an automated procedure to search for and fit the continuum and to measure equivalent widths. We find a ratio $[\text{Fe}/\text{Ni}] = 0.10 \pm 0.05$. Compared with the Galactic trend given by new, high-quality data on

F-, G-, and K-type metal-rich dwarf stars, there is an overabundance, although only at the 1.7σ level.

The significance of the kinematics of Tycho-G is evaluated from the new data. We discuss the probability of its being a metal-rich thick-disk star with a high velocity perpendicular to the Galactic plane and also with a high Ni abundance, and find it to be $P \lesssim 0.00037$. Given the parameters of the orbit and the present radius of the star, its low rotational velocity is well explained, even without considering the removal of angular momentum by the impact of the ejecta.

The position of Tycho-G with respect to the centroid of the X-ray emission of Tycho’s SNR is within the uncertainties affecting the location of the site of the explosion in other SNRs (see also the discussion in RL04). The star’s luminosity is close to the predictions of Pan et al. (2012b), for main-sequence companions of SNe Ia at the age of Tycho. Tycho-G, however, should have already started to evolve away from the main sequence at the time of the explosion.

There is not, at present, any solid argument against Tycho-G being the surviving companion of SN 1572. On the contrary, its kinematic characteristics and distance range strongly point to this conclusion, even in the absence of any Ni enhancement. The alternative possibility, that it is just an interloper found by pure chance has a very low probability. From our survey of the central region of the SNR, we conclude that, apart from Tycho-G, there is no possible candidate for the SN companion. Therefore, if Tycho-G were to be discarded by some future findings, that would favor a double-degenerate system as the origin of SN 1572, as has been plausibly found for SN 1006 (González Hernández et al. 2012; Kerzendorf et al. 2012) and for the progenitor of SNR 0509–67.5 in the LMC (Schaefer & Pagnotta 2012).

Most recent searches for SN Ia companions have either shown their absence or put strong limits on their presence, thus tilting the balance toward the double-degenerate channel. From the metallicity distribution of G-type dwarfs, however, contributions from both the single-degenerate and the double-degenerate channels appear to be necessary (Mennekens et al. 2012). Based on our study, SN 1572 appears to be a very good candidate for the single-degenerate channel.

Hydrodynamic simulations of the impact of SN Ia ejecta on companion stars having already left the main sequence, as well as calculations of their subsequent evolution, are required for additional progress in this field.

11 ACKNOWLEDGMENTS

This work is based on observations with the NASA/ESA *Hubble Space Telescope*, obtained at the Space Telescope Science Institute (STScI), which is operated by AURA, Inc., under NASA contract NAS 5-26555; the specific programs were GO-9729, GO-10098, and GO-12469. P.R.-L. and R.C. acknowledge support from grant AYA2009–13667, financed by the MICINN of Spain. J.I.G.H. received financial support from the Spanish Ministry project MINECO AYA2011–29060, and also from the Spanish Ministry of Economy and Competitiveness (MINECO) under the 2011 Severo Ochoa Program MINECO SEV-2011-0187. A.V.F. is grateful for the support of the Christopher R. Redlich Fund, the TABASGO Foundation, and NSF grants AST-0908886 and

AST-1211916; funding was also provided by NASA grants GO-10098, GO-12469, and AR-12623 from STScI. Some of the data presented herein were obtained at the W. M. Keck Observatory, which is operated as a scientific partnership among the California Institute of Technology, the University of California, and NASA; the observatory was made possible by the generous financial support of the W. M. Keck Foundation. We thank the referee, Wolfgang Kerzendorf, for his careful reading of the manuscript and for useful suggestions that improved our work.

REFERENCES

- Abt H. A., Morrell N. I. 1993, in Peculiar versus Normal Phenomena in A-type and Related Stars (ASP Conf. Ser. 44), ed. M. M. Dworetzky, F. Castelli, R. Faraggiana (San Francisco: ASP), 384
- Abt H. A., Morrell N. I. 1995, *ApJS*, 99, 135
- Anderson J. 2002, in Omega Centauri, A Unique Window into Astrophysics (ASP Conf. Ser. 265), ed. F. van Leeuwen, J. D. Hughes, G. Piotto (San Francisco: ASP), 87
- Anderson J. 2007, Instrument Science Report ACS 2007-08 (Baltimore: STScI)
- Anderson J., Bedin L. 2010, Instrument Science Report ACS2010-03 (Baltimore: STScI)
- Anderson J., Bedin L. R., Piotto G., et al. 2006, *A&A*, 454, 1029
- Anderson J., King I. R. 2006, Instrument Science Report ACS 2006-01 (Baltimore: STScI)
- Anderson J., Piotto G., King, I. R. 2009, *ApJ*, 697, L58
- Anderson J., Sarajedini A., Bedin L.-R., et al. 2008, *AJ*, 135, 2055
- Anderson J., van der Marel R. P. 2010, *ApJ*, 710, 1032 (A10)
- Bedin L.-R., Piotto G., Carraro G., et al. 2006, *A&A*, 460, L27
- Bedin L.-R., Piotto G., King I. R., et al. 2003, *AJ*, 126, 247
- Bellini A., Anderson J., Bedin L.-R. 2011, *PASP*, 123, 622
- Bellini A., Bedin L.-R. 2009, *PASP*, 121, 1419
- Bensby T., Feltzing S., Lundstrom I. 2003, *A&A*, 410, 527
- Binney J., Tremaine S. 2008, *Galactic Dynamics*, 2nd ed. (Princeton: Princeton Univ. Press)
- Branch D., Livio M., Yungelson L. R., et al. 1995, *PASP*, 107, 1019
- Buser R., Rong J., Karaali S. 1999, *A&A*, 348, 98
- Canal R., Mendez J., Ruiz-Lapuente P. 2001, *ApJ*, 550, L53
- Cox C., Gilliland R. L. 2003, in The 2002 HST Calibration Workshop: Hubble after the Installation of the ACS and the NICMOS Cooling System, ed. S. Arribas, A. Koekemoer, B. Whitmore (Baltimore: STScI), 58
- Decourchelle, A., Sauvageot, J. L., Audard, M., et al. 2001, *A&A*, 365, L218
- Edwards Z. I., Pagnotta A., Schaefer B. E. 2012, *ApJ*, 747, L19
- Eggleton P. P. 1983, *ApJ*, 268, 368
- Fuhrmann K. 2005, *MNRAS*, 359, L35
- Fuhrmann, K. 2011, *MNRAS*, 414, 2893
- Gilli G., Israelian G., Ecuivillon A., et al. 2006, *A&A*, 449, 723
- Gilmore G., Wyse R. F. G. 1985, *AJ*, 90, 2015
- González Hernández J. I., Delgado-Mena E., Sousa S., et al. 2013, *A&A*, 552, A6
- González Hernández J. I., Israelian G., Santos N. C., et al. 2010, *ApJ*, 720, 1592
- González Hernández J. I., Ruiz-Lapuente P., Filippenko A. V., et al. 2009, *ApJ*, 691, 1 (GH09)
- González Hernández J. I., Ruiz-Lapuente P., Tabernero H., et al. 2012, *Nature*, 489, 533
- Hughes, J. P. 2000, *ApJ*, 545, L53
- Iben I. Jr., Tutukov A. V. 1984, *ApJS*, 54, 335
- Ihara Y., Ozaki J., Doi M., et al. 2007, *PASJ*, 59, 811
- Jee M. J., Blakeslee J. P., Sirianni M., et al. 2007, *PASP*, 119, 1403
- Kerzendorf W. E., Schmidt, B. P., Asplund M., et al. 2009, *ApJ*, 701, 1665 (K09)
- Kerzendorf W. E., Schmidt B. P., Laird J. B., et al. 2012, *ApJ*, 759, 7
- Kerzendorf W. E., Schmidt B. P., Yong D., et al. 2010, in Progenitors and Environments of Stellar Explosions (<http://www.iap.fr/col2010>)
- Kerzendorf W. E., Yong D., Schmidt B. P., et al. 2013, *ApJ*, 774, ID 99 (K13)
- Krause O., Tanaka M., Usuda T., et al. 2008, *Nature*, 456, 617
- Kurucz R. L., Furenlid I., Brault J., et al. 1984, *Solar Flux Atlas from 296 to 1300 nm*, NOAO Atlas 1 (Cambridge: Harvard Univ. Press)
- Liu Z.-W., Pakmor R., Röpke F. K., et al. 2012, *A&A*, 548, A2
- Liu Z.-W., Pakmor R., Röpke F. K., et al. 2013, *A&A*, 554, A109
- Livio M. 2000, in Type Ia Supernovae, Theory and Cosmology, ed. J. C. Niemeyer, J. W. Truran (Cambridge: Cambridge Univ. Press), 33
- Livio M., Truran J. W. 1992, *ApJ*, 389, 695
- Lu F. J., Wang Q. D., Ge M. Y., et al. 2011, *ApJ*, 732, L11
- Maeda, K., et al. 2010, *ApJ*, 708, 1703
- Marietta E., Burrows A., Fryxell B. 2000, *ApJS*, 128, 615
- Mennekens N., Vanbeveren D., De Greve J. P. 2012, [arXiv:1212.0313](http://arxiv.org/abs/1212.0313)
- Neves V., Santos N. C., Sousa S. G., et al. 2009, *A&A*, 497, 563
- Pakmor R., Hachinger S., Röpke F. K., Hillebrandt W. 2011, *A&A*, 528, A117
- Pan K.-C., Ricker P. M., Taam R. E. 2012a, *ApJ*, 750, 151
- Pan K.-C., Ricker P. M., Taam R. E. 2012b, *ApJ*, 760, 21
- Perlmutter S., Aldering G., Goldhaber G., et al. 1999, *ApJ*, 517, 565
- Podsiadlowski P. 2003, [arXiv:astro-ph/0303660](http://arxiv.org/abs/astro-ph/0303660)
- Reynoso, E. M., Moffett, D. A., Goss, W. M., et al. 1997, *ApJ*, 491, 816
- Riess A. G., Filippenko A. V., Challis P., et al. 1998, *AJ*, 116, 1009
- Robin A. C., Haywood M., Créze M., et al. 1999, *A&A*, 305, 125
- Robin A. C., Reylé C., Derrière S., et al. 2003, *A&A*, 409, 523
- Ruiz-Lapuente P. 1997, *Science*, 276, 1813
- Ruiz-Lapuente P. 2004, *ApJ*, 612, 357
- Ruiz-Lapuente P., Comeron F., Mendez J., et al. 2004, *Nature*, 431, 1069 (RL04)
- Ruiz-Lapuente P., Comeron F., Smartt S., et al. 2003, in From Twilight to Highlight: The Physics of Supernovae, ed. W. Hillebrandt, B. Leibundgut (Berlin: Springer-Verlag), 140
- Schaefer B. E., Pagnotta A. 2012, *Nature*, 481, 164
- Schmidt, B. P., Kerzendorf, W. E., Frebel, A., et al. 2007, in Accretion and Explosion: the Astrophysics of Degenerate Stars (<http://online.itp.ucsb.edu/online/snovae07/schmidt/oh>)
- Shappee B. J., Kochanek C. S., Stanek K. Z. 2013, *ApJ*, 765, 150
- Skrutskie M. F., Cutri R. M., Stiening R., et al. 2006, *AJ*, 131, 1163
- Sousa S. G., Santos N. C., Israelian G., et al. 2007, *A&A*, 469, 783
- Thompson T. A., Gould A. 2012, [arXiv:1210.6050](http://arxiv.org/abs/1210.6050)
- Ubeda L., Anderson J. 2012, AAS Meeting 219, 241.03
- Uchida H., Yamaguchi H., Koyama K. 2013, *ApJ*, 771, 56
- Warren J. S., Hughes J. P., Badenes C., et al. 2005, *ApJ*, 634, 376
- Webbink R. F. 1984, *ApJ*, 277, 355
- Whelan J., Iben I. Jr. 1973, *ApJ*, 186, 1007
- Williams B. J., et al. 2013, [arXiv:1305.0567](http://arxiv.org/abs/1305.0567)
- Winkler P. F., Long K. S., Hamilton A. J. S., et al. 2005, *ApJ*, 624, 189

ID #	2X [pxl]	2Y [pxl]	α [h m s]	δ [° ' '']	$\mu_{\alpha \cos \delta}$ [mas/yr]	$\sigma_{\mu_{\alpha \cos \delta}}$ [mas/yr]	α_0 [mas]	σ_{α_0} [mas]	μ_{δ} [mas/yr]	$\sigma_{\mu_{\delta}}$ [mas/yr]	δ_0 [mas]	σ_{δ_0} [mas]	e_f	N_{used}	P04
(1)	(2)	(3)	(4)	(5)	(6)	(7)	(8)	(9)	(10)	(11)	(12)	(13)	(14)	(15)	(16)
0407	7206.453	4873.601	00:25:20.839	+64:07:23.84	-1.11	0.06	0.29	0.38	0.93	0.08	-0.28	0.52	4	40	AG
0421	7543.742	5010.013	00:25:19.793	+64:07:26.15	-0.38	0.04	0.00	0.28	0.01	0.07	0.06	0.43	4	43	AF
0437	6886.601	5187.700	00:25:21.754	+64:07:30.44	1.26	0.20	0.11	1.20	-0.20	0.26	-0.88	1.60	4	12	AH
0443	6627.324	5251.553	00:25:22.528	+64:07:32.01	1.76	0.28	-0.60	1.70	0.16	0.21	-0.32	1.25	4	36	AI2
0447	6627.897	5273.218	00:25:22.523	+64:07:32.44	73.07	0.09	0.67	0.57	-2.82	0.07	0.14	0.45	4	37	AI1/HP-1
0461	9359.687	5450.838	00:25:14.213	+64:07:32.80	1.07	0.06	-0.16	0.39	-0.05	0.06	-0.16	0.37	4	43	AE
0473	6176.894	5554.506	00:25:23.841	+64:07:38.54	0.18	0.05	0.14	0.32	0.73	0.07	0.22	0.44	4	42	AJ
0478	7689.718	5612.546	00:25:19.245	+64:07:37.94	0.39	0.10	-0.07	0.62	-4.31	0.07	-0.24	0.40	4	19	U
0494	9032.650	5836.380	00:25:15.136	+64:07:40.83	-0.37	0.03	-0.22	0.19	-1.01	0.06	-0.33	0.38	4	38	AB
0521	9342.525	6110.129	00:25:14.149	+64:07:45.90	2.52	0.03	0.06	0.19	-1.75	0.07	0.29	0.46	4	38	Y
0538	9561.368	6307.383	00:25:13.450	+64:07:49.57	0.78	0.04	-0.24	0.27	0.06	0.07	0.12	0.42	4	36	Z
0547	9135.457	6407.250	00:25:14.724	+64:07:52.04	1.32	0.06	-0.08	0.36	-0.26	0.06	0.15	0.35	4	35	X
0549	6479.269	6425.946	00:25:22.772	+64:07:55.49	-0.67	0.08	-0.22	0.47	0.49	0.08	-0.13	0.45	4	38	V
0561	9172.066	6560.786	00:25:14.586	+64:07:55.05	-2.96	0.04	-0.08	0.27	-0.53	0.05	-0.10	0.33	4	38	T
0576	8447.388	6706.630	00:25:16.757	+64:07:58.78	0.69	0.06	-0.25	0.39	-0.20	0.06	-0.36	0.39	4	43	I
0582	6196.793	6736.471	00:25:23.574	+64:08:01.98	-2.63	0.06	0.24	0.33	-3.98	0.04	-0.10	0.26	4	39	G
0585	9583.340	6776.396	00:25:13.301	+64:07:58.85	-1.17	0.07	-0.18	0.42	-0.76	0.04	-0.08	0.28	4	42	AA
0604	10335.937	6957.142	00:25:10.988	+64:08:01.56	-1.12	0.04	0.56	0.27	-2.25	0.07	-0.45	0.44	3	43	AD2
0605	10316.559	6965.116	00:25:11.045	+64:08:01.74	-1.24	0.14	0.18	0.92	-1.58	0.16	0.59	1.03	4	23	AD1
0613	8978.947	7096.368	00:25:15.077	+64:08:05.90	-2.35	0.06	-0.09	0.35	-0.28	0.03	0.12	0.21	4	44	J
0624	7142.628	7237.451	00:25:20.619	+64:08:10.83	-2.03	0.09	-0.05	0.56	-1.28	0.07	-0.34	0.44	4	40	D
0635	7217.616	7312.230	00:25:20.379	+64:08:12.23	-1.98	0.07	0.21	0.41	-1.09	0.06	0.01	0.38	4	40	C1
0636	7211.301	7322.301	00:25:20.396	+64:08:12.44	-1.75	0.07	0.11	0.41	-1.07	0.07	0.01	0.42	4	41	C2
0637	7187.140	7339.344	00:25:20.466	+64:08:12.80	0.08	0.11	0.15	0.63	-0.14	0.10	-0.03	0.61	4	42	C3
0639	10326.291	7373.700	00:25:10.943	+64:08:09.84	-1.09	0.07	0.04	0.43	-0.87	0.04	-0.02	0.25	4	46	AC
0661	7894.163	7545.876	00:25:18.286	+64:08:16.09	1.74	0.05	-0.14	0.29	0.28	0.05	-0.31	0.32	4	44	E
0662	7339.115	7567.867	00:25:19.966	+64:08:17.16	-1.67	0.06	0.09	0.34	0.59	0.08	0.17	0.49	4	17	B
0675	7382.387	7712.681	00:25:19.809	+64:08:19.99	-2.82	0.10	-0.07	0.60	-3.58	0.11	-0.07	0.69	4	17	A2
0724	9026.359	8217.860	00:25:14.735	+64:08:28.11	2.64	0.13	0.36	0.24	0.96	0.04	0.07	0.07	4	29	N
0729	5131.101	8261.419	00:25:26.540	+64:08:33.47	-0.25	0.09	0.33	0.54	0.95	0.08	0.01	0.50	4	32	AK
0731	8244.058	8315.272	00:25:17.090	+64:08:30.95	-3.31	0.15	0.24	0.95	0.25	0.07	-0.28	0.43	4	17	F
0752	8983.145	8521.532	00:25:14.813	+64:08:34.19	1.34	0.09	-0.62	0.57	2.38	0.04	-0.68	0.26	4	44	Q
0754	9319.918	8554.696	00:25:13.786	+64:08:34.46	3.68	0.09	0.03	0.56	0.93	0.05	-0.11	0.34	4	47	S
0758	8748.322	8568.527	00:25:15.517	+64:08:35.39	-0.18	0.10	0.07	0.58	0.25	0.05	0.23	0.30	4	45	R
0762	5987.199	8604.576	00:25:23.884	+64:08:39.30	0.24	0.12	-0.21	0.73	0.03	0.07	-0.34	0.42	4	37	K
0768	5847.235	8658.103	00:25:24.299	+64:08:40.53	0.36	0.12	0.02	0.72	-0.08	0.04	-0.13	0.25	4	39	L
0775	9043.112	8696.190	00:25:14.600	+64:08:37.59	-0.27	0.20	-0.60	1.17	-1.64	0.21	-1.06	1.22	4	43	P2
0782	9055.353	8761.868	00:25:14.552	+64:08:38.88	1.39	0.36	0.66	2.39	0.20	0.09	0.53	0.59	4	15	P1
0790	9033.674	8838.131	00:25:14.604	+64:08:40.41	5.13	0.20	0.08	1.29	2.85	0.14	-0.08	0.92	4	15	O
0819	7749.819	9140.564	00:25:18.444	+64:08:47.91	-3.19	0.07	0.05	0.43	-0.84	0.03	0.00	0.19	4	50	H
0832	8140.813	9296.019	00:25:17.231	+64:08:50.54	-0.61	0.12	-0.24	0.78	0.44	0.08	0.12	0.48	4	49	M
0833	6219.594	9306.132	00:25:23.056	+64:08:52.96	-1.36	0.10	-0.10	0.60	-0.60	0.10	0.42	0.61	4	36	AM
0835	6581.337	9354.961	00:25:21.951	+64:08:53.51	-0.31	0.09	-0.17	0.57	0.09	0.04	0.04	0.24	4	38	W
0837	6159.991	9383.838	00:25:23.224	+64:08:54.57	-0.14	0.09	0.34	0.58	-0.35	0.09	0.24	0.55	4	41	AL
0873	7134.303	9951.594	00:25:20.169	+64:09:04.72	-2.83	0.11	0.42	0.73	-0.96	0.05	-0.02	0.32	4	43	AN

Table 2. Extract of our catalog for the sources in common with those in P04. A full version of this Table (from 0001 to 1148) is provided as supplementary electronic material of this work.

<i>Star</i>	<i>B</i> [mag]	<i>V</i> [mag]	<i>R</i> [mag]	μ_b [mas/yr]	<i>d</i> [kpc]	v_r [km/s]	v_α [km/s]	v_δ [km/s]
(1)	(2)	(3)	(4)	(5)	(6)	(7)	(8)	(9)
A	14.82±0.03	13.29±0.03	12.24±0.03	-0.88±0.90	1.1±0.3	-23±1	-0.5±3	-4.6±5
B	16.35±0.03	15.41±0.03	–	0.76±0.08	2.6±0.5	-38±8	-20.6±4	7.3±1.5
C1	21.06±0.12	19.06±0.05	17.77±0.03	-0.88±0.06	0.75±0.5	-33±6	-4.7±3.5	-0.4±0.9
C2	22.91±0.20	20.53±0.15	–	-0.88±0.07	~40	–	~300	~200
D	22.97±0.28	20.70±0.10	19.38±0.06	-1.06±0.07	0.8±0.2	-50.6±0.8	-7.7±1.9	-4.8±0.12
E	21.24±0.13	19.79±0.07	18.84±0.05	0.10±0.05	>20	-26±18	≥-95	≥27
F	19.02±0.05	17.73±0.03	16.94±0.03	0.59±0.07	1.5±0.5	-34±11	-23.5±8	1.8±0.6
G	20.09±0.08	18.71±0.04	17.83±0.03	-3.69±0.04	2.5-5.0	-80±0.5	-31/-62	-47/-95
H	21.39±0.14	19.80±0.07	18.78±0.05	-0.51±0.03	≈1.8/~24	-71±10	≈-27/~-360	≈-7/~-96
I	–	21.75±0.16	20.36±0.09	-0.27±0.06	≈4	–	≈13	≈-4
J	21.15±0.12	19.74±0.07	18.84±0.05	-0.04±0.03	≈9	-45±6	≈-100	≈-12
K	21.64±0.15	20.11±0.08	19.15±0.05	0.01±0.07	≈2.4/~27	-33±10	2.7/31	0.3/4
L	22.77±0.26	21.08±0.12	20.00±0.07	-0.12±0.04	≈4	–	≈7	≈-1.5
M	23.49±0.36	21.82±0.16	20.72±0.10	0.50±0.08	≈4	–	≈12	≈8
N	19.59±0.06	18.29±0.04	17.47±0.03	0.68±0.04	≈1.5-2	-30±6	≈19-25	≈7-9
O	18.62±0.04	17.23±0.03	16.37±0.03	2.31±0.14	<1	-15±7	<24	<13
P	–	17.61±0.03	16.78±0.03	0.06±0.09	≈1	-36±10	≈7	≈1
Q	22.35±0.21	20.59±0.09	19.41±0.06	2.23±0.04	≈2	–	≈13	≈23
R	22.91±0.28	21.38±0.13	20.26±0.08	0.27±0.05	3.3±0.2	–	-2.8±1.8	3.9±0.3
S	–	21.30±0.13	19.74±0.07	0.55±0.05	1.3±0.1	–	23±2	6±1
T	21.82±0.17	20.23±0.08	19.20±0.05	-0.22±0.05	≈2/~30	–	≈-28	≈-5
U	19.03±0.05	17.73±0.03	16.95±0.03	-4.33±0.07	≈1	-38±4	≈2	≈-20
V	23.32±0.33	21.41±0.13	20.20±0.08	0.56±0.08	≈3	–	≈-9.5	≈7
W	22.13±0.19	20.44±0.09	19.27±0.05	0.12±0.04	≈2	–	≈-3	≈1

Table 3. *BVR* photometry, proper motions perpendicular to the Galactic plane, distances, radial velocities, and tangential velocity components of the 24 stars with $m_V \leq 22$ mag, located within 42 arcsec from the X-ray centroid of Tycho’s SNR.